

Half-quantum mirror Hall effect

Received: 25 September 2023

Accepted: 1 August 2024

Published online: 13 August 2024

 Check for updatesBo Fu¹, Kai-Zhi Bai² & Shun-Qing Shen^{2,3}  


We predict a half-quantized mirror Hall effect induced by mirror symmetry in strong topological insulator films. These films are known to host a pair of gapless Dirac cones in the first Brillouin zone associated with surface electrons. Our findings reveal that mirror symmetry assigns a unique mirror parity to each Dirac cone, resulting in a half-quantized Hall conductance of $\pm \frac{e^2}{2h}$ for each cone. Despite the total electrical Hall conductance being null due to time-reversal invariance, the difference in the Hall conductance between the two cones yields a quantized Hall conductance of $\frac{e^2}{h}$ for the difference in mirror currents. The effect of helical edge mirror current - a crucial feature of this quantum effect - may, in principle, be determined by means of electrical measurements. The half-quantum mirror Hall effect reveals a type of mirror-symmetry induced quantum anomaly in a time-reversal invariant lattice system, giving rise to a topological metallic state of matter with time-reversal invariance.

In the quantum field theory, the coupling of a single flavor of 2+1d massless Dirac fermions to a U(1) gauge field results in a topological Chern–Simons term for the gauge field, which corresponds to a half-quantized Hall conductance. This phenomenon explicitly violates parity and time-reversal symmetries, leading to the emergence of parity anomaly^{1,2}. Due to this anomaly, a single Dirac cone theory cannot have an ultraviolet completion without breaking parity symmetry. In other words, the anomaly can be viewed as an obstruction to regularizing a continuum Dirac theory on a lattice without breaking symmetry or gauge invariance. In lattice crystals, the bandwidth of the band structure is finite, and the lattice spacing provides a natural ultraviolet cutoff for the wave vector. As a result, massless Dirac cones always appear in pairs in lattice systems with time-reversal symmetry to avoid quantum anomaly. For instance, graphene exhibits a pair of massless Dirac cones³, in addition to the double degeneracy of electron spin, while a strong topological insulator (TI) film hosts a pair of surface massless Dirac fermions^{4–6}.

The quest to realize parity anomaly in condensed matter has been ongoing since the early 1980s^{7,8}. The primary approach involves introducing a symmetry-breaking term to open an energy gap in the Dirac fermions^{8–13}. For example, Haldane⁸ proposed a periodic alternating magnetic flux in a graphene lattice to enforce gap opening in paired Dirac cones, while Yu et al.¹⁰ suggested doping transition metal elements into a magnetically ordered TI film. These predictions have led to the observation of the quantum anomalous Hall effect^{14–18}, with

numerous efforts continuing to explore quantum anomaly in condensed matter^{19–24}. Another approach involves realizing a single gapless Dirac cone on a lattice, which breaks time-reversal symmetry to circumvent fermion doubling and results in a half-quantized Hall conductance²⁴. A recent measurement of the half-quantized Hall effect in a semimagnetic topological insulator²² revealed the signature of parity anomaly of a single Dirac cone in a parity anomalous semimetal^{25,26}. A theoretical work based on the Landauer–Büttiker formula highlights the importance of the dephasing process in understanding this effect²⁷. Additionally, the chiral edge current of a parity anomalous semimetal has been reported in an electrical circuits experiment²⁸.

A key question is whether it is possible to directly observe parity anomaly in a time-reversal invariant system without introducing symmetry-breaking perturbations, despite the constraint of symmetry. The surface states of a topological insulator are regarded as a promising platform for realizing parity anomaly in condensed matter. However, a film of TI necessarily possesses two surfaces, where the anomalous terms from each surface alternate in sign, effectively canceling each other out. In this study, we report the finding of a quantum anomaly in a mirror-symmetric TI film with time-reversal invariance. In addition to time-reversal symmetry, certain strong TIs, such as Bi₂Te₃ and Bi₂Se₃, exhibit additional mirror planes perpendicular to specific axes. It is feasible to grow or to fold mechanically a thin film with a twin boundary that respects both mirror and time-reversal symmetry.

¹School of Sciences, Great Bay University, Dongguan 523000 Guangdong Province, China. ²Department of Physics, The University of Hong Kong, Pokfulam Road, Hong Kong, China. ³Quantum Science Center of Guangdong-Hong Kong-Macau Greater Bay Area, Shenzhen, China.  e-mail: sshen@hku.hk

Consequently, a mirror parity can be assigned to the two independent Dirac cones, leading to a quantum anomaly for each cone with a half-quantized Hall conductance of $\pm \frac{e^2}{2h}$. Although the total electric Hall conductance is zero due to time-reversal invariance, the difference in the Hall conductance between the two cones results in a quantized Hall conductance $\frac{e^2}{h}$ for the difference in mirror currents. This phenomenon is termed the half quantum mirror Hall effect. The helical edge mirror current, a key feature of this quantum effect, can be measured through transport measurements using entirely electrical means.

Results

The mirror symmetry and single gapless Dirac cones

The surface of a \mathbb{Z}_2 strong topological insulator hosts an odd number of gapless Dirac surface cones as a consequence of the bulk-surface correspondence^{4,5,29}. For simplicity, we consider only the case of one gapless Dirac surface cone. In this scenario, a TI film hosts a pair of gapless surface states separated spatially if we assume the film is thick enough such that the finite size effect can be ignored³⁰. Denote the Hamiltonian \mathcal{H} for the quasi-two-dimensional system, which can be viewed as a semimetal with its degenerated low-energy spectra consisting of doubled Dirac fermions. As the system does not break the time-reversal symmetry, the appearance of the paired Dirac cones does not cause any quantum anomaly in general if the two bands away from the Dirac point or at the higher energy part are inseparable.

The presence of the mirror symmetry in the z -direction $\widehat{\mathcal{M}}_z$ (perpendicular to the film as shown in the left panel of Fig. 1) leads to a further classification of the band structure^{31–36}. $\widehat{\mathcal{M}}_z$ is an inversion operator under the sign flip of the Cartesian coordinate component perpendicular to the mirror plane, $(r_x, r_y, r_z) \rightarrow (r_x, r_y, -r_z)$. Mirror symmetry also applies a 180-degree rotation about the z -axis to the electron spin, so $\widehat{\psi}_\uparrow \rightarrow -i\widehat{\psi}_\uparrow$ and $\widehat{\psi}_\downarrow \rightarrow i\widehat{\psi}_\downarrow$ such that the operator

squares to -1 for spin one-half fermions, $\widehat{\mathcal{M}}_z^2 = -1$. The mirror symmetry means $[\widehat{\mathcal{H}}, \widehat{\mathcal{M}}_z] = 0$, which implies that all the states of the quasi-2D system can be labeled with a mirror eigenvalue $\pm i$ as shown in Fig. 1 (middle panel). Thus, we can utilize the mirror symmetry to define a projection operator denoted as $\widehat{\mathcal{P}}_\chi$, with the expression $\widehat{\mathcal{P}}_\chi = \frac{1}{2}(1 - i\chi\widehat{\mathcal{M}}_z)$ where χ represents the eigenvalue of the mirror symmetry operation $\widehat{\mathcal{M}}_z$. By utilizing the projection operator, the Hamiltonian $\widehat{\mathcal{H}}$ can be decomposed into the two distinct sectors, $\widehat{\mathcal{H}}_+$ and $\widehat{\mathcal{H}}_-$ where each sector $\widehat{\mathcal{H}}_\chi$ is given by $\widehat{\mathcal{H}}_\chi = \widehat{\mathcal{P}}_\chi \widehat{\mathcal{H}} \widehat{\mathcal{P}}_\chi$. The time-reversal symmetry $\widehat{\mathcal{T}}$ commutes with any spatial symmetry $[\widehat{\mathcal{T}}, \widehat{\mathcal{M}}_z] = 0$, thus the two sectors are the time-reversal counterpart of each other $\widehat{\mathcal{T}}\widehat{\mathcal{H}}_\chi\widehat{\mathcal{T}}^{-1} = \widehat{\mathcal{H}}_{-\chi}$, but each $\widehat{\mathcal{H}}_\chi$ breaks the time-reversal symmetry. Since there exists a pair of the gapless Dirac fermions within the bulk gap of a strong TI, we come to draw a conclusion that *for a mirror-symmetric TI film, each sector $\widehat{\mathcal{H}}_\chi$ hosts a single gapless Dirac cone in the first Brillouin zone which is the spatial mixture of the top and bottom surface states with even or odd mirror parity.*

Existence of a single massless Dirac cone in each $\widehat{\mathcal{H}}_\chi$ means to have parity anomaly. The half-quantized Hall conductance is associated to each mirror sector $\sigma_{xy}^\chi = \frac{\chi}{2} \frac{e^2}{h}$ as a consequence of the quantum anomaly of massless Dirac fermions^{24,26}. The time-reversal symmetry requires the co-existence of two flavors of massless Dirac fermions with $\chi = +1$ and -1 , and the total Hall conductance $\sigma_{xy}^H = \sum_\chi \sigma_{xy}^\chi = 0$. However, their difference defines a nontrivial mirror Hall conductance, $\sigma_{xy}^{Mz} = \sum_\chi \chi \sigma_{xy}^\chi = \frac{e^2}{h}$. The mirror Hall effect is quite similar to the quantum spin Hall effect^{37,38}, but the mirror Hall conductance is only one-half of quantum spin Hall effect. Hence we term this phenomenon as the “half-quantum mirror Hall effect”. It is a metallic or semi-metallic phase as the Fermi level always crosses the conduction or valence bands of the massless Dirac fermions, which is essentially distinct from the quantum spin Hall effect. From the band theory in solid, the factor $\frac{\chi}{2}$

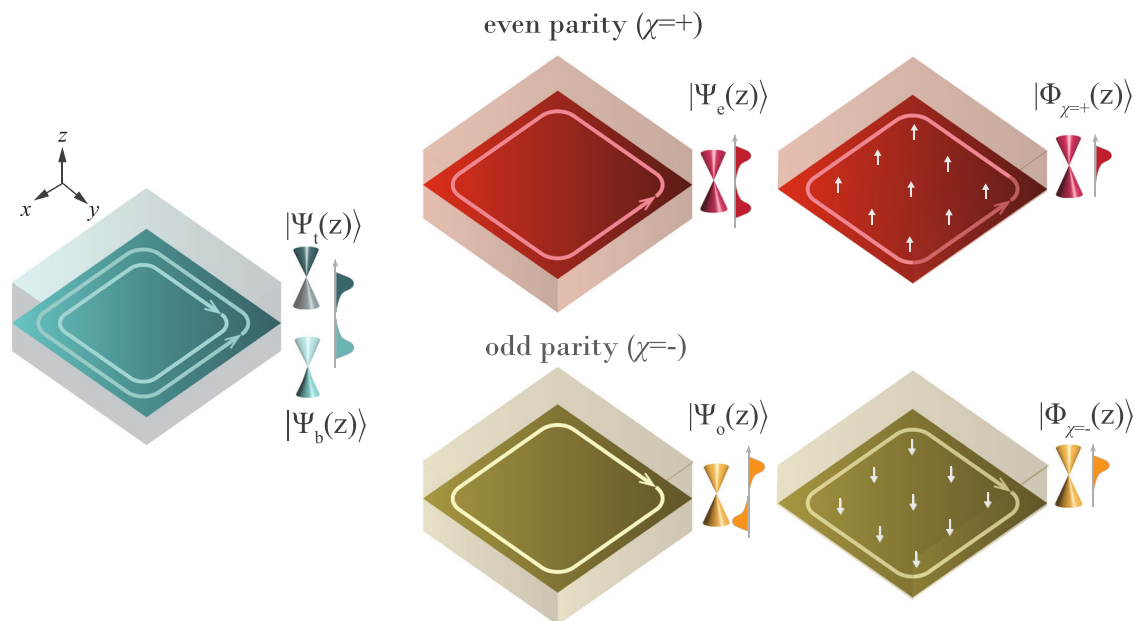


Fig. 1 | Schematic of separation of a time-reversal invariant system with mirror symmetry into two symmetry broken subsystems with mirror parity. (Left panel) The time-reversal invariant system is represented by the cyan color, with the wave functions of the Dirac states on the top and bottom surfaces denoted by $|\Psi_{t/b}\rangle$, respectively. The presence of mirror symmetry connects these two states: $iU_{M_z}|\Psi_t(z)\rangle = |\Psi_b(-z)\rangle$. The cyan-colored circles with arrows indicate the helical mirror current centered at the mirror plane. (Middle panel) The system characterized by definite mirror parity, features a single Dirac cone within the Brillouin zone. The wavefunction of surface states exhibits either even ($\chi = +1$, red color) or odd ($\chi = -1$, yellow color) parity with respect to the z -axis, which is represented by

$|\Psi_{e/o}(z)\rangle = \frac{1}{\sqrt{2}}(|\Psi_t(z)\rangle \pm |\Psi_b(z)\rangle)$, respectively. (Right panel) After transitioning to the eigenbasis of mirror operator $\widehat{\phi}_{z,\chi} = \widehat{\psi}_z \mp i\chi U_{M_z} \widehat{\psi}_{-z}$, each mirror eigensector is equivalent to a topological insulator thin film with a single surface subjected to a symmetry-breaking term. The wavefunction of the surface state, denoted by $|\Phi_\chi(z)\rangle$, is distributed on a single surface within the new coordinate framework. The red and yellow circles with arrows represent the counter-propagating mirror current $J_{\chi=\pm}$ associated with the half-quantum mirror Hall effect. The arrows pointing along the z -direction indicate the effective magnetization on the surface in the mirror eigenbasis.

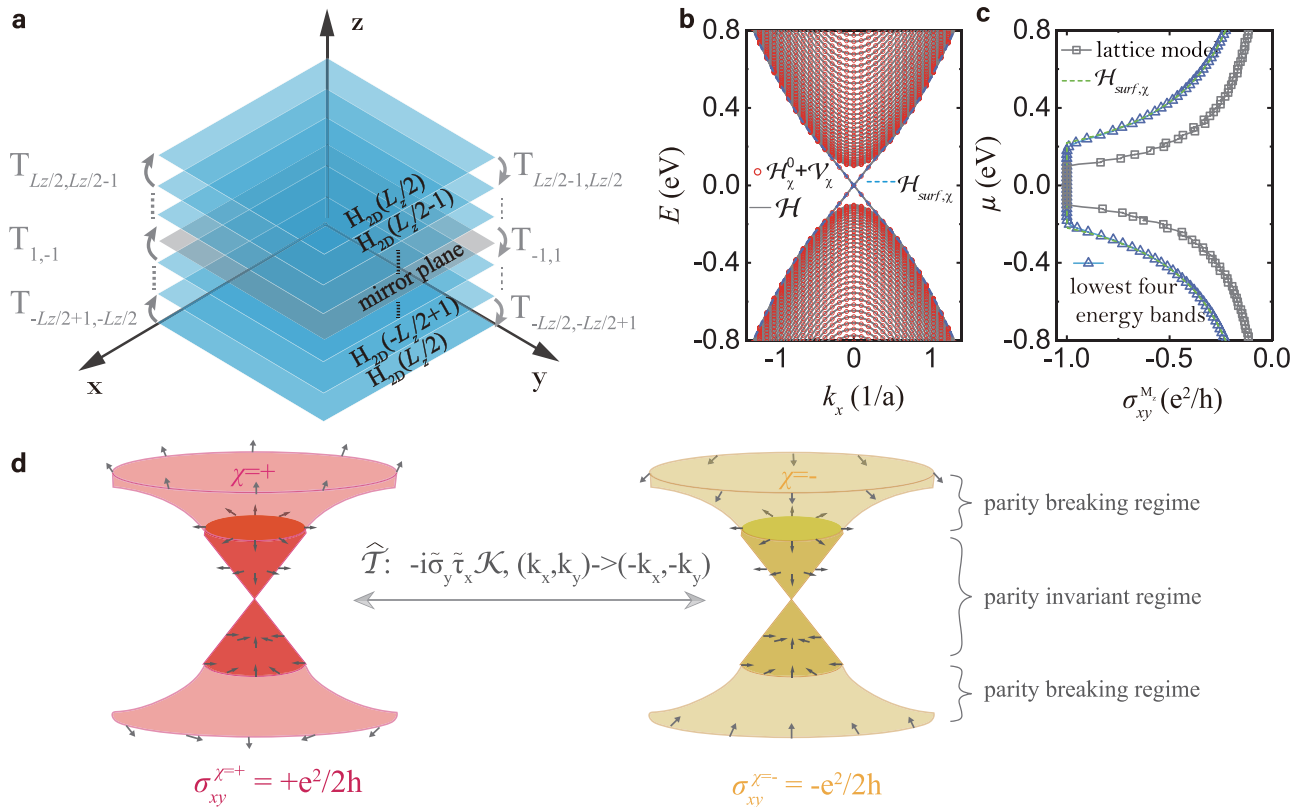


Fig. 2 | Symmetry-breaking gapless Dirac cones and half-quantum mirror Hall effect. **a** Schematic diagram of a film exhibiting mirror symmetry. $H_{2D}(z) = H_0 + \sum_{\delta=\hat{x},\hat{y}} (H_{\delta} e^{i\delta \cdot \mathbf{k}} + \text{h.c.})$ represents the Hamiltonian of each layer, while $T_{z,z+1}$ and $T_{z+1,z}$ represent the hopping terms between adjacent layers in the z -direction. The gray plane represents the mirror plane. **b** The band structure of topological insulator thin film (gray lines) is based on a 3D tight-binding model calculation with open boundary conditions parallel to the mirror plane and periodic boundary conditions along the remaining two directions. The red circles represent the energy spectrum by diagonalizing the Hamiltonian describing half thickness of the film (\hat{H}_{χ}^0) with a time-reversal symmetry breaking term \hat{v}_{χ} on the bottom layer. The blue dashed lines are from the effective Hamiltonian [Eq. (7)]. **c** The mirror Hall conductance as a function of chemical potential μ calculated by using Eq. (8) based

on the 3D tight-binding model for TI and the model for the surface states in Eq. (7). The blue line marked with triangles represents the contributions from the lowest-energy four gapless bands as determined by the tight-binding model. **d** Schematic diagram of two separated classes of the gapless Dirac cones with even and odd parity. Black arrows represent the pseudo-spin texture (i.e., $\hat{\mathbf{d}} = (\vec{\sigma})$) of two gapless Dirac cones with opposing mirror eigenvalues $i\chi$. The time-reversal symmetry \hat{T} transforms one Dirac cone into another with the opposite mirror eigenvalue. For each mirror sector, we can define a parity operator \hat{M} , which transforms $(k_x, k_y) \rightarrow (-k_x, k_y)$ and is represented by $i\hat{\sigma}_y$ in the 2×2 subspace. This parity symmetry is disrupted in high-energy states (indicated by light colors) but is preserved in low-energy states (indicated by dark colors).

is closely associated to the band structure of the massless Dirac cone²⁴. Thus, the mirror symmetry-induced quantum anomaly also defines a unique type of quantum anomalous semimetal with time-reversal invariance.

Mirror plane with time-reversal symmetry breaking

The time-reversal symmetry breaking in the sector \hat{H}_{χ} is attributed to the existence of the mirror plane in a strong topological insulator system, which can be regarded as an origin of quantum anomaly. Consider the Hamiltonian of a topological insulator thin film stacked along z direction in the real-space representation (\mathbf{r}, z) with $\mathbf{r} = (x, y)$,

$$\hat{H} = \sum_{\mathbf{r},z} \left[\hat{\psi}_{\mathbf{r},z}^{\dagger} H_0(z) \hat{\psi}_{\mathbf{r},z} + \left(\sum_{\delta=\hat{x},\hat{y}} \hat{\psi}_{\mathbf{r},z}^{\dagger} H_{\delta}(z) \hat{\psi}_{\mathbf{r}+\delta,z} + \hat{\psi}_{\mathbf{r},z}^{\dagger} T_{z,z+1} \hat{\psi}_{\mathbf{r},z+1} + \text{h.c.} \right) \right] \tag{1}$$

where the creation field operator $\hat{\psi}_{\mathbf{r},z}^{\dagger}$ is a vector representing the internal degrees of freedom in the unit cell, including orbit and spin. $H_0(z)$ denotes the on-site Hamiltonian matrix and $H_{\delta}(z)$ represents the hopping matrix that characterizes electron transitions between adjacent sites along x or y direction, corresponding to the displacement vectors $\delta = \hat{x}$ or \hat{y} , respectively. $T_{z,z+1}$ and $T_{z,z+1}^{\dagger}$ corresponds to

the hopping terms between adjacent layers in the z -direction. h.c. is an abbreviation for ‘‘Hermitian conjugate’’. For a thin film with an even number of layers L_z , as the mirror plane located at the center of the middle two layers, the indices z are sequentially labeled as $-L_z/2, \dots, -1, 1, \dots, L_z/2$ as illustrated in Fig. 2a. The mirror symmetry \hat{M}_z along z -axis transforms the creation and the annihilation operators as

$$\begin{aligned} \hat{M}_z : \hat{\psi}_{\mathbf{r},z}^{\dagger} &\rightarrow \hat{\psi}_{\mathbf{r},-z}^{\dagger} U_{M_z}^{\dagger}, \\ \hat{M}_z : \hat{\psi}_{\mathbf{r},z} &\rightarrow U_{M_z} \hat{\psi}_{\mathbf{r},-z}. \end{aligned} \tag{2}$$

Here U_{M_z} is a unitary matrix representation of \hat{M}_z on the space of one site. If the system exhibits the mirror symmetry along z -axis, such that $\hat{M}_z^{-1} \hat{H} \hat{M}_z = \hat{H}$, then the following constraints hold:

$$\begin{aligned} U_{M_z}^{\dagger} H_0(z) U_{M_z} &= H_0(-z), \\ U_{M_z}^{\dagger} T_{z,z+1} U_{M_z} &= T_{-z-1,-z}^{\dagger}. \end{aligned} \tag{3}$$

Owing to the translational invariance in $x-y$ plane, we can apply the Fourier transformation $\hat{\psi}_{\mathbf{k},z} = \frac{1}{\sqrt{L_x L_y}} \sum_{\mathbf{r}} e^{-i\mathbf{k} \cdot \mathbf{r}} \hat{\psi}_{\mathbf{r},z}$ where $L_x \times L_y$ is the number of sites for each layer. Subsequently, by introducing

$\hat{\Psi}_{\mathbf{k}}^\dagger = [\hat{\psi}_{\mathbf{k}, -\frac{L_z}{2}}, \hat{\psi}_{\mathbf{k}, -\frac{L_z}{2}+1}, \dots, \hat{\psi}_{\mathbf{k}, \frac{L_z}{2}-1}, \hat{\psi}_{\mathbf{k}, \frac{L_z}{2}}]^\dagger$, the Hamiltonian is expressed as $\hat{\mathcal{H}} = \sum_{\mathbf{k}} \hat{\Psi}_{\mathbf{k}}^\dagger H(\mathbf{k}) \hat{\Psi}_{\mathbf{k}}$ where $H(\mathbf{k})$ is a block tridiagonal matrix with respect to the layer index. In this framework, the mirror symmetry operator is represented by $\mathcal{M}_z = U_{M_z} \otimes I_A$, where I_A the anti-diagonal identity matrix, whose dimension corresponds to the number of layers. It can be straightforwardly verified that $\mathcal{M}_z^{-1} H(\mathbf{k}) \mathcal{M}_z = H(\mathbf{k})$ by utilizing relations in Eq. (3). Since $[H(\mathbf{k}), \mathcal{M}_z] = 0$, \mathcal{M}_z and $H(\mathbf{k})$ can be diagonalized simultaneously. Consequently, the degenerate energy eigenstates of $H(\mathbf{k})$ for each wave vector \mathbf{k} can be distinguished by their eigenvalues of the mirror operator \mathcal{M}_z , which are $i\chi$ with $\chi = \pm 1$.

To more clearly comprehend the physical origins of the symmetry-breaking term within each mirror sector, we can construct an eigenbasis of mirror operator from Eq. (2)

$$\hat{\phi}_{r,z,\chi}^\dagger = \frac{1}{\sqrt{2}} (\hat{\psi}_{r,z}^\dagger + i\chi \hat{\psi}_{r,-z}^\dagger U_{M_z}^\dagger). \quad (4)$$

Considering that the mirror symmetry relates z to $-z$ in a nonlocal manner, the two bases are constructed by employing symmetry-related pairs of unit cells located at z and $-z$. In the eigenbasis, the Hamiltonian $\hat{\mathcal{H}}$ can be divided into two sectors, such that $\hat{\mathcal{H}} \equiv \sum_{\chi} \hat{\mathcal{H}}_{\chi}$, with each sector acting on states for which the operator $\hat{\mathcal{M}}_z$ has eigenvalues of $\pm i$. The Hamiltonian for each χ sector reads as $\hat{\mathcal{H}}_{\chi} = \hat{\mathcal{H}}_{\chi}^0 + \hat{\mathcal{V}}_{\chi}$, the time-reversal invariant part $\hat{\mathcal{H}}_{\chi}^0$ is identical to one-half of $\hat{\mathcal{H}}$ in which all the field operators $\{\hat{\psi}_{r,z}^\dagger, \hat{\psi}_{r,z}\}$ are replaced by the eigenbasis $\{\hat{\phi}_{r,z,\chi}^\dagger, \hat{\phi}_{r,z,\chi}\}$ with $z \geq 1$ to avoid the double counting. The extra term is $\hat{\mathcal{V}}_{\chi} = -i\chi \sum_r \hat{\phi}_{r,1,\chi}^\dagger T_{-1,1} U_{M_z} \hat{\phi}_{r,1,\chi}$ where $T_{-1,1}$ represents the hopping matrix connecting the neighboring layers $z=1$ and $z=-1$ around the mirror plane. To be more precise, we employ the widely-used Bernevig–Hughes–Zhang (BHZ) model to describe the Hamiltonian for topological insulators^{12,39,40} and illustrate the results. See Supplementary Note 1 for details of the model. This model exhibits horizontal mirror symmetry with $U_{M_z} = -i\sigma_z \tau_z$ and $T_{-1,1} = t_{\perp} \sigma_0 \tau_z - i \frac{\lambda_{\perp}}{2} \sigma_z \tau_x$. Here, τ_z takes values of ± 1 corresponding to two distinct orbital states and $\sigma_z = +1(-1)$ for spin up (down) along z direction. Subsequently, $\hat{\mathcal{V}}_{\chi}$ takes the form:

$$\hat{\mathcal{V}}_{\chi} = -\chi \sum_r \hat{\phi}_{r,1,\chi}^\dagger (t_{\perp} \sigma_z \tau_0 - \frac{\lambda_{\perp}}{2} \sigma_0 \tau_y) \hat{\phi}_{r,1,\chi}. \quad (5)$$

The first term is equivalent to a Zeeman field along the z direction and the second term represents an antiferromagnetic order which is staggered along z direction and uniform within xy -plane^{41,42}, both breaking time-reversal symmetry explicitly. An intuitive explanation for the emergence of the symmetry-breaking in the mirror eigenbasis can be described as follows: The spin behaves as a pseudo-vector or axial vector, which means that under mirror symmetry, its component parallel to the mirror plane is inverted, while the component perpendicular to the plane remains unchanged. From Eq. (4), two in-plane spins with opposite orientations located at positions symmetric with respect to a mirror plane can be arranged to maintain mirror symmetry. However, the existence of a horizontal mirror symmetry $\hat{\mathcal{M}}_z$ requires that the spin polarization on self-reflected surfaces be oriented out-of-plane within each mirror sector. The symmetry broken term $\hat{\mathcal{V}}_{\chi}$ makes it possible that there exists a single Dirac cone in the first Brillouin zone in $\hat{\mathcal{H}}_{\chi}$ on a lattice (see the right panel of Fig. 1). As shown in Fig. 2b, we plot the energy spectrum of the TI film calculated using the tight-binding model [Eq.(1)] with a thickness of $L_z=80$, shown in gray solid lines. Alongside, we show the spectrum of the

Hamiltonian $\hat{\mathcal{H}}_{\chi}$ in the mirror eigenbasis (red circles), which considers a halved thickness of $L_z/2 = 40$ and extra symmetry-breaking term [Eq. (5)] on one surface. Remarkably, the two spectra coincide. Since the spectra of $\hat{\mathcal{H}}_{\chi=+}$ and $\hat{\mathcal{H}}_{\chi=-}$ are degenerate, we present only the results for $\hat{\mathcal{H}}_{\chi=+}$ in Fig. 2b.

Gapless Dirac cones with parity symmetry breaking

We then develop a gapless Dirac cone model for mirror-symmetric topological insulator thin film to elucidate the fundamental physics underlying the half-quantum mirror Hall effect. Our focus is on the geometry depicted in Fig. 2a, which is characterized by an open boundary condition along the z -axis and periodic boundary conditions in the xy -plane. The system's Hamiltonian can be decomposed into two separate parts: $H(\mathbf{k}) = H_{1d}(\mathbf{k}) + H_{\parallel}(\mathbf{k})$, both exhibiting mirror symmetry. $H_{1d}(\mathbf{k})$ is a one-dimensional lattice model for topological insulator film with a momentum-dependent gap $M_0(\mathbf{k}) + 2t_{\perp}$. $H_{\parallel}(\mathbf{k})$ is block-diagonalized within the layer space. We first address the eigenproblem of $H_{1d}(\mathbf{k})$, where the eigenvalue equation is given by $H_{1d}(\mathbf{k}) |\Phi_{n,\zeta,\chi,\mathbf{k}}\rangle = \zeta \Delta_n(\mathbf{k}) |\Phi_{n,\zeta,\chi,\mathbf{k}}\rangle$ with $|\Phi_{n,\zeta,\chi,\mathbf{k}}\rangle$ being the eigenvectors and $\zeta \Delta_n(\mathbf{k})$ the corresponding eigenvalues with $\zeta = \pm$ and $n = 1, 2, 3, \dots, L_z$. $i\chi = \pm i$ represent the mirror eigenvalues of the degenerate energy eigenstates of $H_{1d}(\mathbf{k})$ for each wave vector \mathbf{k} , i.e. $\mathcal{M}_z |\Phi_{n,\zeta,\chi,\mathbf{k}}\rangle = i\chi |\Phi_{n,\zeta,\chi,\mathbf{k}}\rangle$. Upon obtaining the eigenstates of $H_{1d}(\mathbf{k})$, we proceed to project the remaining part of the Hamiltonian $H_{\parallel}(\mathbf{k})$ onto this basis. In the eigenproblem, we aim to determine a solution of the form $\Phi(z) - e^{i\xi z} \Phi(0)$ where ξ is a general complex number. The z -component of spin is conserved for $H_{1d}(\mathbf{k})$: $[H_{1d}(\mathbf{k}), \sigma_z] = 0$. Moreover, since the spin z operator σ_z commutes with the mirror symmetry operator \mathcal{M}_z (i.e., $[\sigma_z, \mathcal{M}_z] = 0$), σ_z and \mathcal{M}_z can be diagonalized simultaneously. This allows the eigenstates to be redefined as $|\Phi_{n,\zeta,s,\mathbf{k}}\rangle = |\Phi_{n,\zeta,\mathbf{k}}^s\rangle \otimes |s\rangle$ where $|s\rangle$ is an eigenstate of σ_z with eigen values $s = \pm$, such that $\sigma_z |s\rangle = s |s\rangle$. The corresponding eigen equation for the spatial components $\Phi_{n,\zeta,\mathbf{k}}^s(z)$ becomes

$$\left\{ [M_0(\mathbf{k}) + 2t_{\perp} \cos \xi] \tau_z + s \frac{\lambda_{\perp}}{2} \tau_x \sin \xi \right\} \Phi_{n,\zeta,\mathbf{k}}^s(z) = \zeta \Delta_n(\mathbf{k}) \Phi_{n,\zeta,\mathbf{k}}^s(z). \quad (6)$$

If ξ solves this equation, then $-\xi$ is also a solution. By substituting general solutions that adhere to the boundary condition into the eigenequations, we derive a set of equations that are self-contained and can be solved to determine the eigenvalues $\zeta \Delta_n(\mathbf{k})$ and also the corresponding eigenstates $|\Phi_{n,\zeta,\mathbf{k}}^s\rangle$. We ascertain that these eigenstates are indeed the eigenfunctions of the mirror operator: $\mathcal{M}_z |\Phi_{n,\zeta,s,\mathbf{k}}\rangle = -is \zeta |\Phi_{n,\zeta,s,\mathbf{k}}\rangle$. Given that $H_{\parallel}(\mathbf{k})$ is invariant under mirror symmetry: $[\mathcal{M}_z, H_{\parallel}(\mathbf{k})] = 0$, also considering that it flips the spin, the projection onto these eigenbasis reveals that only the states with opposite ζ and opposite spin configuration have non-zero overlap: $\langle \Phi_{n',\zeta',s',\mathbf{k}} | H_{\parallel}(\mathbf{k}) | \Phi_{n,\zeta,s,\mathbf{k}} \rangle = \lambda_{\parallel} \delta_{\zeta',-\zeta} \delta_{n',n} [\sin(k_x) \sigma_x + \sin(k_y) \sigma_y]_{s',s}$. Therefore, the Hamiltonian $H_{\parallel}(\mathbf{k})$ couples basis states with opposite spins within the same mirror eigensector. See the Methods section and Supplementary Note 2 for further details.

After projection, we identify a series of Dirac bands: four are gapless, while the remaining bands are gapped and topologically trivial. The topological phenomena manifest in the four gapless bands; here, the low-energy states correspond to surface states, and the high-energy states within these bands transition to bulk states (as shown in Supplementary Fig. 2). In the eigenbasis of mirror symmetry, the wave functions of the surface states in each sector $\hat{\mathcal{H}}_{\chi}$ are symmetric ($\chi = +1$) or antisymmetric ($\chi = -1$) about z , in which the sites z and $-z$ are connected and breaks the locality property on the lattice. By solving the three-dimensional model for a TI film, we find it essential to incorporate a term that breaks the symmetry to provide and accurate

representation of the surface states²⁶:

$$H_{\text{surf},\chi} = \lambda_{\parallel} \sin k_x \tilde{\sigma}_x + \lambda_{\parallel} \sin k_y \tilde{\sigma}_y + \chi \Delta(\mathbf{k}) \tilde{\sigma}_z \quad (7)$$

where the Pauli matrices $\tilde{\sigma}$ act on the spaces spanned by $[\Phi_{n=1,\zeta=+,\chi=+}, \Phi_{n=1,\zeta=-,\chi=+}]$ and $[\Phi_{n=1,\zeta=+,\chi=-}, \Phi_{n=1,\zeta=-,\chi=-}]$ for the $\chi=+$ and $\chi=-$ sectors respectively and $\Delta(\mathbf{k}) = \Theta[-m_0(\mathbf{k})]m_0(\mathbf{k})$ with $\Theta(x)$ as a step function and $m_0(\mathbf{k}) = m_0 - 4t_{\parallel}(\sin^2 \frac{k_x}{2} + \sin^2 \frac{k_y}{2})$. m_0 is the bulk gap of TI. For each mirror sector χ , we can define a parity operator \hat{M} , which transforms $(k_x, k_y) \rightarrow (-k_x, k_y)$ and is represented by $i\tilde{\sigma}_y$ in the 2×2 subspace. In the vicinity of $\mathbf{k} = 0$, when $m_0(\mathbf{k}) > 0$, $\Delta(\mathbf{k})$ is zero, allowing $H_{\text{surf},\chi}$ to preserve the parity symmetry. Conversely, in high energy states when $m_0(\mathbf{k}) < 0$, $\Delta(\mathbf{k}) \simeq m_0(\mathbf{k}) \neq 0$, explicitly breaking the parity symmetry. For the details of the derivation, see Supplementary Information. With the inclusion of the symmetry-breaking term, the gapless states described by the Hamiltonian in Eq. (7) diverge significantly from the conventional Dirac surface states^{5,43}. As shown in Fig. 2d, we present a schematic diagram to illustrate the main difference between the proposed gapless Dirac cone model with broken parity symmetry (\tilde{M}) and the conventional Dirac surface states: in the parity invariant regime ($m_0(\mathbf{k}) > 0$), the pseudo-spin texture is confined to the xy -plane, whereas outside this regime, the pseudo-spin texture acquires z components that break the parity symmetry explicitly. The time-reversal symmetry, which is antiunitary, commutes with the mirror symmetry: $[\hat{T}, \hat{M}_z] = 0$. Then for an eigenstate $|\psi_{\chi}\rangle$ of \hat{M}_z that satisfies $\hat{M}_z|\psi_{\chi}\rangle = i\chi|\psi_{\chi}\rangle$, it follows that $\hat{M}_z\hat{T}|\psi_{\chi}\rangle = \hat{T}\hat{M}_z|\psi_{\chi}\rangle = -i\chi\hat{T}|\psi_{\chi}\rangle$. This implies that after the transformation of \hat{T} , the state $|\psi_{\chi}\rangle$ flips its eigenvalue of \hat{M}_z , $\hat{T}|\psi_{\chi}\rangle \sim |\psi_{-\chi}\rangle$.

Therefore, the time-reversal symmetry \hat{T} maps one mirror sector onto the other. In Fig. 2b, the spectrum of the four-band Hamiltonian [Eq.(7)] are plotted as blue dashed lines, demonstrating that it accurately reproduces the spectrum not only at low energies but also at the corners of the Brillouin zone (as shown in Supplementary Fig. 1). In this way, a single Dirac cone may exist in the first Brillouin zone as a consequence of the symmetry breaking to avoid the fermion doubling problem⁴⁴. This is distinct from the conventional effective model for the surface states which is only valid for a small k ⁴³. As explained in Supplementary Note 3, we elucidate the relationship and distinction between our lattice-based theory and the quantum anomaly originating from an effective $k \cdot p$ model. The mass term can be interpreted as a natural regularization that emerges on a lattice and resolves the divergence in the charge-charge and mirror-mirror polarization tensors inherent in the effective $k \cdot p$ model. Additionally, it serves as the topological origin of the half-quantum mirror Hall effect.

We note that prior research by Creutz and Horváth⁴⁵ has similarly examined topological systems in film geometry. However, in contrast with our research, we note significant distinctions. Reference⁴⁵ explored 1+D (D=1,3)-a dimensional film without time-reversal symmetry and featuring chiral surface states, while our study investigates three-dimensional topological insulator film with time-reversal symmetry and characterized by helical surface states. Consequently, the models in these works fall into two distinct topological classes, leading to fundamentally different quantum anomalies: ref. 45 addresses the chiral anomaly, while our work is focused on the parity anomaly. Reference⁴⁵ has primarily focused on the low-energy surface states, claiming that the degeneracy between a pair of gapless Dirac fermions cancels the anomaly. In contrast, our study classifies Dirac cones according to parity by utilizing mirror symmetry, revealing the persistence of the parity anomaly. This method not only reveals the full energy dispersions for each class but also highlights the critical role of

mirror symmetry in generating quantum anomaly phenomena within the topological insulator thin film.

Quantum mirror Hall conductance

The intrinsic mirror Hall conductance can be evaluated by means of the Kubo formula in the linear response theory⁴⁶⁻⁴⁸,

$$\sigma_{xy}^{M_z} = \frac{2e\hbar}{L_x L_y} \sum_{\mathbf{k}, n \neq m} f(\epsilon_n) \frac{\text{Im} \langle u_{n\mathbf{k}} | \hat{J}_{M_z, x} | u_{m\mathbf{k}} \rangle \langle u_{m\mathbf{k}} | v_y | u_{n\mathbf{k}} \rangle}{(\epsilon_n - \epsilon_m)^2} \quad (8)$$

where n, m are the band indices, the velocity operator at each \mathbf{k} is given by $v_i = \frac{1}{\hbar} \frac{\partial H(\mathbf{k})}{\partial k_i}$ with $i = x, y$ and $\hat{J}_{M_z} = ie\mathcal{M}_z \mathbf{v}$ is the mirror current operator, $|u_{n\mathbf{k}}\rangle$ is the eigenvector of $H(\mathbf{k})$ with the eigen-energy as $\epsilon_n(\mathbf{k})$ and $f(\epsilon_n) = \Theta(\mu - \epsilon_n)$ is the Fermi-Dirac distribution at zero temperature with μ as the chemical potential. By using the mirror operator's eigenbasis, denoted by $|u_{n\mathbf{k}}^{\chi}\rangle$ with $\mathcal{M}_z |u_{n\mathbf{k}}^{\chi}\rangle = i\chi |u_{n\mathbf{k}}^{\chi}\rangle$, the Kubo formula for $\sigma_{xy}^{M_z}$ can be recast as $\sigma_{xy}^{M_z} = \frac{e^2}{\hbar} \sum_{\chi, n, \mathbf{k}} \chi f(\epsilon_n^{\chi}(\mathbf{k})) \Omega_n^{\chi}(\mathbf{k})$ where $\Omega_n^{\chi}(\mathbf{k}) = 2\text{Im} \langle \partial_x u_{n\mathbf{k}}^{\chi} | \partial_y u_{n\mathbf{k}}^{\chi} \rangle$ is the mirror-resolved Berry curvature for each state. Each mirror sector $\hat{\mathcal{H}}^{\chi}$ belongs to the class A of topological classifications, enabling the association of an anomalous Hall conductance σ_{xy}^{χ} with it, and the mirror Hall conductance can be expressed as $\sigma_{xy}^{M_z} = \sum_{\chi} \chi \sigma_{xy}^{\chi}$. Since $\hat{\mathcal{H}}^{\chi}$ contains a single gapless Dirac cone in the whole Brillouin zone, the Stoke's theorem allows the Berry curvature integral over the occupied states to be converted into a line integral of the Berry connection along the Fermi surface (FS) for a partially filled band n : $\sigma_{xy, n}^{\chi} = \frac{e^2}{2\pi\hbar} \int d^2 \mathbf{k} \Omega_n^{\chi}(\mathbf{k}) \Theta(\mu - \epsilon_n^{\chi}) = \frac{e^2}{2\pi\hbar} \oint_{\text{FS}} d\mathbf{k} \cdot \mathcal{A}_n^{\chi}(\mathbf{k})$ where $\mathcal{A}_n^{\chi}(\mathbf{k}) = -i \langle u_{n\mathbf{k}}^{\chi} | \partial_{\mathbf{k}} | u_{n\mathbf{k}}^{\chi} \rangle$ denotes the Berry connection⁴⁹. If Fermi surface consists of a single gapless Dirac cone, the Berry phase around the Fermi surface is quantized to π . As a result, the Hall conductance is half quantized $\sigma_{xy}^{\chi} = \chi \frac{e^2}{2\hbar}$ when the chemical potential is located within the bulk gap²⁶. The half-quantum mirror Hall effect can also be interpreted using the gapless Dirac cone model presented in Eq. (7). The Hall conductance of a generic two-band Hamiltonian $H_{\text{surf},\chi}(\mathbf{k}) = \mathbf{d}_{\chi}(\mathbf{k}) \cdot \boldsymbol{\sigma}$ is given by $\sigma_{xy}^{\chi} = \frac{e^2}{\hbar} \frac{1}{4\pi} \int d^2 \mathbf{k} [\Theta(\mu - |\mathbf{d}_{\chi}|) - \Theta(\mu + |\mathbf{d}_{\chi}|)] \hat{\mathbf{d}}_{\chi} \cdot (\partial_{k_x} \hat{\mathbf{d}}_{\chi} \times \partial_{k_y} \hat{\mathbf{d}}_{\chi})$, which represents the coverage of the unit vector $\hat{\mathbf{d}}_{\chi}(\mathbf{k}) = \mathbf{d}_{\chi}(\mathbf{k}) / |\mathbf{d}_{\chi}(\mathbf{k})|$ across the Bloch sphere for the occupied states. The Hamiltonian corresponds to vectors $\mathbf{d}_{\chi}(\mathbf{k}) = (\lambda_{\parallel} \sin k_x, \lambda_{\parallel} \sin k_y, \chi \Delta(\mathbf{k}))$. At $\mathbf{k} = (\pi, \pi)$, the unit vector $\hat{\mathbf{d}}_{\chi}(\mathbf{k}) = (0, 0, \chi \text{sgn}(\Delta(\pi, \pi)))$ points to the north (south) pole on the unit sphere for $\chi = +1$ ($\chi = -1$), assuming $\text{sgn}(\Delta(\pi, \pi)) > 0$. For wavevectors on the Fermi surface in the vicinity of the Dirac points, the unit vector $\hat{\mathbf{d}}_{\chi}(\mathbf{k}) = (\lambda_{\parallel} \sin k_x, \lambda_{\parallel} \sin k_y, 0)$ resides in the equatorial plane of the unit sphere. As depicted in Fig. 2d, this configuration of $\hat{\mathbf{d}}_{\chi}(\mathbf{k})$ spans half of the unit sphere, resulting in a winding number of $\chi/2$, which corresponds to a Hall conductance of $\sigma_{xy}^{\chi} = \chi \frac{e^2}{2\hbar}$. Then, the mirror Hall conductance is quantized, $\sigma_{xy}^{M_z} = \sigma_{xy}^{\chi=+} - \sigma_{xy}^{\chi=-} = \frac{e^2}{\hbar}$. To further validate it, we calculate the mirror Hall conductance as a function of the chemical potential μ using Eq. (8) based on the tight-binding model, shown as the black line with squares in Fig. 2c. The green dashed line is according to the gapless Dirac model in Eq. (7). For comparison, we also present the contributions from the four lowest-energy gapless bands within the tight-binding model, indicated by the blue line marked with triangles. They show good agreement with each other. Apart from the four gapless bands with $n = 1$, all other bands are gapped and topologically trivial (when chemical potential lies within their gaps, the mirror Hall conductivity is zero), however, they also contribute when chemical potential shifts into the bulk states (i.e., $|\mu| > |m_0|$). The contributions from $n = 3, 4, \dots, L_z$ bands

should also be summed to produce the final results indicated by the black line with squares.

Transport signature

The half-quantum mirror Hall effect is very similar to the spin Hall effect in the semiconductor and can be measurable by full electric means^{50–54}. We consider a two-terminal transport measurement and a charge current is driven between injector and collector electrodes by an electric field. We first examine a system with no coupling between two mirror sectors, where each sector individually satisfies the equation $\sum_j \sigma_{ij}^X E_j = J_i^X$ with $i, j = x, y$. When an external electric field E_y is applied in the y -direction, electrons with opposite mirror eigenvalues acquire anomalous transverse velocities in opposite directions. This results in a transverse current that causes charge to accumulate along the lateral edges of the material, leading to the development of an internal electric field E_x^X in the x -direction for each mirror sector. This electric field opposes further accumulation of charge thereby reaching an equilibrium. At equilibrium, the net transverse current becomes zero (i.e., $J_x^X = 0$), which allows us to determine the equilibrium self-building electric field as $E_x^X = -E_y \frac{\sigma_{xy}^X}{\sigma_{xx}^X}$. Electrons with opposite mirror eigenvalues accumulate on opposite edges of the material, leading to a spatially varying mirror polarization density $\delta n_{M_z}(x)$, as illustrated in Fig. 3a. Consequently, the self-building electric fields for each mirror sector are oriented in opposite directions. This self-building electric field E_x^X then induces a Hall current in the y -direction, described by $J_{c,y}^{\text{MH}} = \sum_X \sigma_{yx}^X E_x^X$. To compute the total longitudinal charge (c) current $J_{c,y}$ we sum the conductive current from the surface states, $J_{c,y}^{\text{SS}} = \sum_X \sigma_{yy}^X E_y$ with the inverse Hall current, yielding $J_{c,y} = E_y \sum_X (-\sigma_{yx}^X \frac{\sigma_{xy}^X}{\sigma_{xx}^X} + \sigma_{yy}^X)$. The charge current contains two parts $J_{c,y} = J_{c,y}^{\text{SS}} + J_{c,y}^{\text{MH}}$: the first term $J_{c,y}^{\text{SS}}$ comes from the conducting surface states and the second term $J_{c,y}^{\text{MH}}$ arises from the spatial accumulation of the mirror polarization density and is an effect due to the existence of the mirror Hall effect. This mirror Hall-mediated charge transport can be understood as follows: the electric field first induces a mirror charge accumulation on the boundary via the mirror Hall effect and then is converted into the charge current along the electric field via the inverse mirror Hall effect^{55–57}. By making further assumption that $\sigma_{xx}^X = \sigma_{yy}^X$, the two terminal resistances measured, as depicted in the upper panel of Fig. 3b, can be expressed as:

$$R = \frac{L}{W\sigma_c} \left[1 + \tan^2(\theta_{M_z}) \right]^{-1} \quad (9)$$

where we introduce the mirror Hall angle $\theta_{M_z} = \tan^{-1}(\sigma_{xy}^{M_z}/\sigma_c)$ with $\sigma_c = \sum_X \sigma_{xx}^X$ as the total longitudinal charge conductivity and employ the relation $|\tan(\theta_{M_z})| = |\sigma_{xy}^X/\sigma_{xx}^X|$. Next, we will consider the effects of scattering between the two mirror sectors. In this situation, by solving the combined equations of generalized Ohm's law and continuity equations for currents^{58–61}, subject to appropriate boundary conditions, the mirror polarization density and the charge current density are found to be (see Methods)

$$\delta n_{M_z}(x) = -\frac{\sigma_{xy}^{M_z} E_y l_{M_z}}{D_c} \frac{\sinh(x/l_{M_z})}{\cosh(W/2l_{M_z})}, \quad (10)$$

$$J_{c,y}(x) = \sigma_c E_y \left[1 + \tan^2(\theta_{M_z}) \frac{\cosh(x/l_{M_z})}{\cosh(W/2l_{M_z})} \right] \quad (11)$$

for $|x| \leq W/2$ and 0 for outside the system. l_{M_z} is the inter-mirror scattering length and D_c is the charge diffusion constant. We assume inter-mirror scattering time is much longer than the scattering time

within the same mirror eigenvalues such that $l_{M_z} \gg l_e$ where l_e is the mean-free path. To ensure the diffusive transport is 2D, the width is also required to be much longer than a mean-free path, i.e. $W \gg l_e$. Depending on the relative amplitude of l_{M_z} and W , we have two regimes: (i) the weak inter-mirror scattering regime $l_{M_z} \gg W \gg l_e$, the polarization density variation $\delta n_{M_z}(x) \simeq -\sigma_{xy}^{M_z} E_y x/D_c$ shows a linear behavior along the direction perpendicular to the electric field and independent on l_{M_z} and the induced charge current is uniformly distributed in the sample which are shown by the black lines in Fig. 3c,d respectively; (ii) the strong inter-mirror scattering regime $W \gg l_{M_z} \gg l_e$, the boundary effect becomes dominate that mirror charge accumulates at the boundaries and $J_{c,y}^{\text{MH}}$ only flows near the boundaries as shown by the red lines in Fig. 3c and d respectively. As depicted in upper panel of Fig. 3b, the total charge current can be obtained by integrating the current density over the width $I_{c,y} = \int_{-W/2}^{W/2} dx J_{c,y}(x)$ and the voltage drops over the length L of the system is $V = E_y L$. From Eq. (11), the two-terminal measurement resistance $R = V/I_{c,y}$ can be expressed as

$$R = \frac{L}{W\sigma_c} \left[1 + \tan^2(\theta_{M_z}) \frac{\tanh(W/2l_{M_z})}{W/2l_{M_z}} \right]^{-1}. \quad (12)$$

By varying the chemical potential μ through a gate voltage, σ_c can be monotonically tuned to the minimal value $\sigma_{\text{min}} = \frac{2e^2}{\pi h}$ at the Dirac point^{62,63}. While the gate voltage has little impact on the half-quantum mirror Hall effect as its root lies in the quantum anomaly of gapless Dirac bands and is contributed by the deep-lying states. As shown in Fig. 3e, we plot R as a function of μ for different l_{M_z}/W . For $l_{M_z} \gg W$, the mirror eigenvalue can be viewed as a good quantum number, Eq. (12) is then reduced to Eq. (9) as $\frac{\tanh(W/2l_{M_z})}{W/2l_{M_z}} \sim 1$. In this case, as μ moves away from the Dirac point, R initially rises, subsequently peaks when $\sigma_c = |\sigma_{xy}^{M_z}|$, and ultimately decreases, as shown by the darkest green line. As the hybridization between two mirror sectors becomes stronger, l_{M_z} reduces, leading to a decreased contribution from the mirror Hall effect, as described by Eq. (12). When l_{M_z}/W approaches zero, R converges to the transport behavior associated with conventional Dirac surface states in the absence of the mirror Hall effect^{64,65}, as shown by the darkest red line. The resistivity $R_0 = L/W\sigma_c$ can be measured by using conventional six-probe measurement. Thus the value of $\sigma_{xy}^{M_z}$ can be deduced from the measurement of R if the exact mirror symmetry nearly holds (i.e., $l_{M_z} \rightarrow \infty$).

We next consider a multi-terminal measurement and the current I is applied along the y -direction, flowing from from terminal 8 to terminal 2, as depicted in the lower panel of Fig. 3b. The detailed calculations for this setup are provided in "Methods". Here we consider the weak inter-mirror scattering regime $l_{M_z} \gg L, W$. For practical analysis, we derive the analytical expressions in certain limiting cases: (i) In the regime where $x \gg l_{M_z}$, the nonlocal resistivity associated with the mirror Hall effect

$$R_{\text{NL}}(x) \simeq \frac{1}{\sigma_c} \frac{L}{2\xi_w} \frac{\tan^2(\theta_{M_z})}{1 + \tan^2(\theta_{M_z})} e^{-x/\xi_w} \quad (13)$$

with $\xi_w = l_{M_z} \sqrt{1 + \tan^2(\theta_{M_z})}$. (ii) Conversely, for $L, W \gg x$, we have $\omega(k) \simeq l_{M_z}^{-1}$ and the boundary condition along x -direction becomes negligible. Under these conditions, Eq. (28) can be approximated by its value at $x = 0$,

$$R_{28,28} \simeq \frac{L}{W\sigma_c} \frac{\mathcal{F}(\frac{L}{W})}{[1 + \tan^2(\theta_{M_z})]} \quad (14)$$

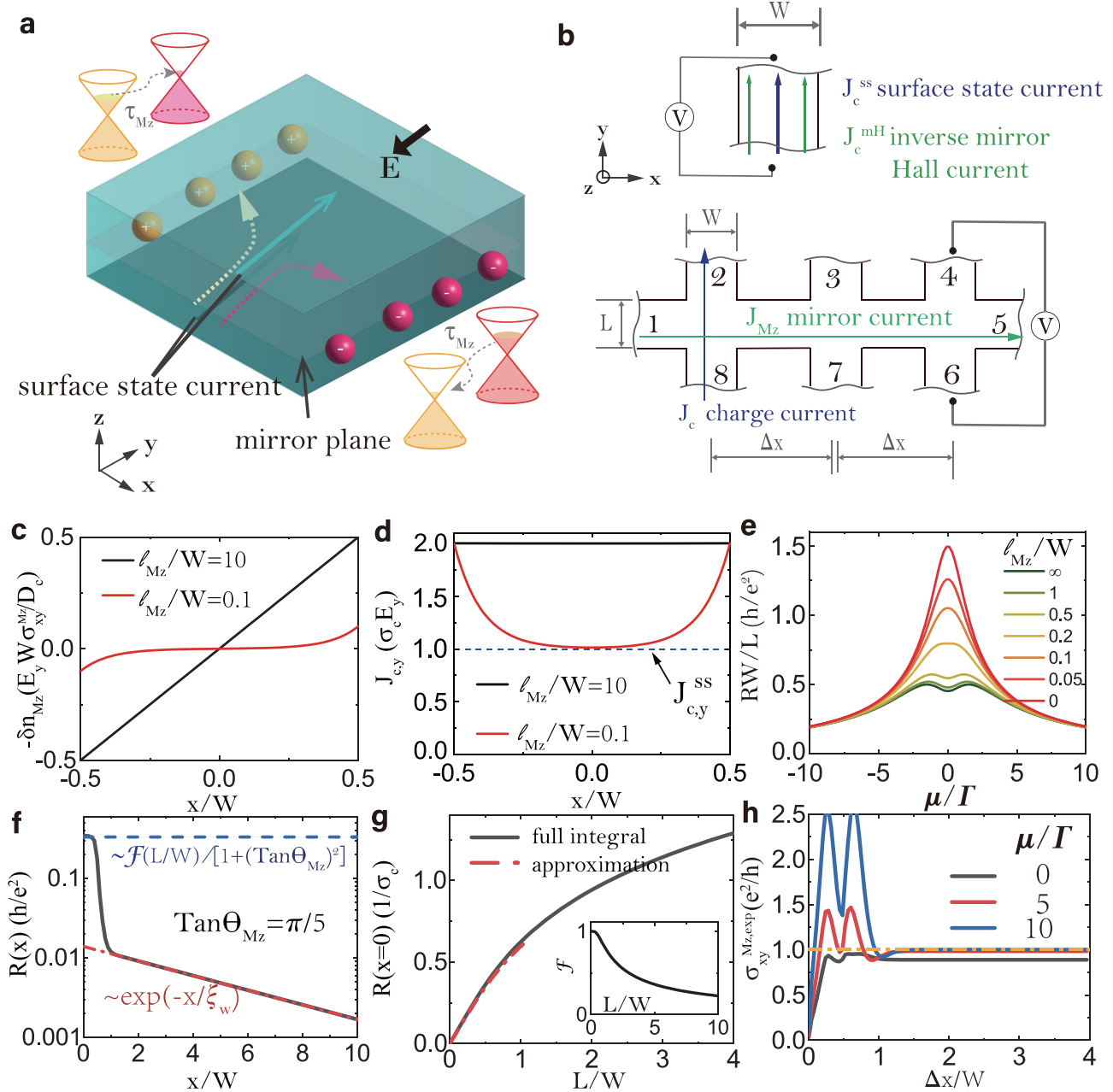


Fig. 3 | Transport signatures of the half-quantum mirror Hall effect. **a** Schematic of mirror Hall effect analyzed in this work. The electrons in $\chi=+$ and $\chi=-$ sectors are denoted by the red and yellow filled circles, respectively. The symbol “E” stands for the in-plane electric field. The arrows with solid lines represent the currents generated by the conducting surface states, while the arrows with dashed lines indicate the mirror Hall current. τ_{M_z} denotes the scattering time between two mirror sectors. **b** A sketch of the two-terminal transport setup and multi-terminal transport setup. W represents the width of the lead, L the height of the sample, and Δx the distance between two neighboring leads. **c** The spatial distributions of polarization density between mirror eigenvalue sectors δn_{M_z} , and **d** the charge current density $J_{c,y}$ in two limiting regimes. The Blue dashed line in panel **d** represents the current density contributed by the conducting surface states. **e** The two terminal resistances as a function of chemical potential E for different relative ratios l_{M_z}/W . The longitudinal conductivity of Dirac surface states can be

calculated by $\sigma_c = \frac{e^2}{\pi h} [1 + (\frac{\mu}{\Gamma} + \frac{\Gamma}{\mu}) \arctan(\frac{\mu}{\Gamma})]$. Γ is the imaginary part of the self-energy around the Dirac point which can be determined within self-consistent Born approximation. **f** The resistance $R(x)$ as a function of the probe position x according to Eq. (28) (black line). The red dashed line represents the nonlocal resistivity obtained when the voltage measurement is taken at a location sufficiently distant from the current injection terminal, as described by Eq. (13). The blue dashed line corresponds to the approximation result given by Eq. (14), which applies when voltage measurement is conducted at the current injection terminal. **g** $R(x=0)$ as a function of L/W from Eq. (13) (black solid line) and Eq. (14) (red dashed line). The inset displays \mathcal{F} versus L/W . Here we use $\tan \theta_{M_z} = \pi/5$. **h** The measured mirror Hall conductivity from Eq. (17) calculated from Eq. (28) for different chemical potentials. We have adopted W as the unit of length. For Fig. f, g, and h, we have set $l_{M_z}/W = 4$. In Fig. f and h, a ratio of $L/W = 0.3$ is utilized.

which is similar to the two-terminal case except for a sample-sized dependent renormalization factor $\mathcal{F}(y) = \text{Re} \sum_{s=\pm} \frac{s}{\pi^2} (\text{Li}_2(e^{-s\pi/y}) - 4\text{Li}_2(e^{-s\pi/5}))$ where Li_2 is the polylogarithm function of order two. We present a plot of the resistivity as a function of the probe position x based on the full integral in Eq. (28) in Fig. 3f. As demonstrated, the

numerical results are in good agreement with the analytical expression given in Eq. (13) when the voltage -measuring probes are positioned significantly far from the terminals where the current is injected. We additionally plot the resistivity as a function of the sample aspect ratio L/W when voltage measurement probes are located at the terminals

where the current the current is injected, as depicted in Fig. 3g. It is evident that when $L \ll W$, the results from the full integral are consistent well with approximation given by Eq. (14). Notably, as L/W approaches zero, we find that \mathcal{F} tends towards unity, and $R_{28,28}$ simplifies to the expression in Eq. (9).

Finally, we address the question of how to extract the half-quantum mirror Hall conductivity from electrical measurements. In experiments, there are three unknown parameters that need to be determined: the longitudinal conductivity σ_c , the mirror Hall conductivity $\sigma_{xy}^{M_z}$, and the inter-mirror scattering length l_{M_z} . Therefore, at least three measurements are necessary. Firstly, according to Eq. (13), ξ_w can be deduced through two nonlocal voltage measurements. These measurements are taken between terminals 3 and 7, and between terminals 4 and 6, which are at distances Δx and $2\Delta x$ from the current injection terminals 2 and 8, respectively, as illustrated in the lower panel of Fig. 3b. From these measurements, ξ_w which is can be extracted by using the relation $\xi_w = \Delta x / \ln(R_{37,28}/R_{46,28})$. Then from Eq. (14), after conducting a two-terminal measurement, the mirror Hall angle can be determined by the following equation:

$$\tan(\theta_{M_z}^{\text{exp}}) = \sqrt{\frac{2\Delta x R_{37,28}^2 / (R_{28,28} R_{46,28})}{W \ln(R_{37,28}/R_{46,28})}} \quad (15)$$

The superscript “exp” indicates the experiment measurement results, which are used to distinguish them from the theoretical predictions. The mirror Hall conductivity and longitudinal conductivity can be determined from the measured data using

$$\sigma_c^{\text{exp}} = \frac{1}{R_{28,28}} \frac{L}{W} \frac{1}{1 + \tan^2(\theta_{M_z}^{\text{exp}})} \quad (16)$$

and

$$\sigma_{xy}^{M_z, \text{exp}} = \frac{1}{R_{28,28}} \frac{L}{W} \frac{\tan(\theta_{M_z}^{\text{exp}})}{1 + \tan^2(\theta_{M_z}^{\text{exp}})} \quad (17)$$

By following this procedure, the desired electrical properties can be accurately determined from the measured values. We employ Eq. (28) to assess the validity of Eq. (17). As depicted in Fig. 3h, when the two nonlocal measurements are taken at a sufficient distance from the current injection terminal, the extracted mirror Hall conductivity approached quantized theoretical prediction over a wide range of energies.

Measuring lattice-symmetry-protected topological responses may not be straightforward, but exploring other lattice-symmetry-protected transport responses can shed light on mirror symmetry-related effects. Take the SnTe class of topological crystalline insulators, for example, which exhibit nonzero mirror Chern numbers, guaranteeing the existence of topological surface states. Quantum coherent magnetotransport measurements have revealed multiple unique Dirac surface states in these materials⁶⁶. Another example is the Bi₄Br₄ compound, protected by C₂ rotation symmetry, which has been classified as a higher-order topological insulator and is expected to host 1D helical hinge states. Recent experimental magnetoresistance measurements have shown pronounced Aharonov–Bohm oscillations, providing evidence for the quantum transport response of topological hinge modes⁶⁷.

Material candidates

The strong 3D TIs Bi₂Te₃ and Bi₂Se₃ have the rhombohedral structure⁶⁸. The bulk structure is constructed by the hexagonal monatomic crystal planes which are stacked along the c-axis in ABC order³⁹. Units of Te(Se)-Bi-Te(Se)-Bi-Te(Se) form a quintuple layer (QL). The coupling is covalent between atomic planes within a QL whereas weak between adjacent QLs, predominantly of the van der Waals type. The crystal structure belongs to the space group $R\bar{3}m$ (No. 166), which

has the Bi atoms situated at 6c(0, 0, ±0.4005), the type-1 Te/Se atoms (Te1/Se1) at 6c(0, 0, ±0.2097), and type-2 Te/Se atoms (Te2/Se2) at 3a(0, 0, 0) Wyckoff positions with $a = 4.38 \text{ \AA}$ and $c = 30.49 \text{ \AA}$. The generators of the space group are (i) the identity \hat{E} , (ii) threefold rotation symmetry \hat{C}_{3z} along the z-axis, (iii) twofold rotation symmetry \hat{C}_{2x} along the x-axis, (iv) inversion symmetry \hat{P} , and (v) a fractional translation $\hat{\tau}_{\frac{2}{3}\frac{1}{3}}$. The combination of the inversion and the twofold rotation symmetry gives rise a mirror symmetry $\hat{M}_x = \hat{C}_{2x}\hat{P}$. The threefold rotation symmetry about the z-axis produces two other mirror symmetries. Hence there are a total of three mirror planes in Bi₂Te₃ which are perpendicular to [110], [100] and [010] axes, respectively. To calculate the electronic structure of a slab geometry along the [100] direction with mirror symmetry as depicted in Fig. 4a, we utilize a tight-binding model comprising eight states with the model parameters are determined by fitting the electronic properties obtained from first principle calculations⁶⁹. These states are denoted as $|P1^+, \pm \frac{1}{2}\rangle$, $|P2^+, \pm \frac{1}{2}\rangle$, $|P2^-, \tilde{\Gamma}_4\rangle$, $|P2^-, \tilde{\Gamma}_5\rangle$, and $|P2^-, \pm \frac{1}{2}\rangle$. Among these states, $|P1^+, \pm \frac{1}{2}\rangle$, $|P2^+, \pm \frac{1}{2}\rangle$ are responsible for the band inversion^{40,69}. The remaining four bands exhibit substantially lower energies compared to the former four bands. The inclusion of these additional four bands only modifies the dispersion and will not influence the band inversion. Consequently, we focus solely on the four bases $|P1^+, \pm \frac{1}{2}\rangle$, $|P2^+, \pm \frac{1}{2}\rangle$ in the following calculations. The form of the Hamiltonian is highly constrained by crystal symmetries and time-reversal symmetry \hat{T} . These symmetry operations are represented by the following unitary operators in the four bases we considered: $\hat{C}_{3z} : e^{-i\frac{2\pi}{3}\sigma_z}$, $\hat{C}_{2x} : -i\sigma_x\tau_z$, $P : \tau_z$ and $\hat{T} : i\sigma_y K$ where the Pauli matrices σ and τ operate on the spin and orbital subspaces, respectively. Hence the mirror symmetry about [100] axis is represented as $\hat{M}_x : -i\sigma_x$. The energy spectrums based on this slab geometry are presented in Fig. 4b. The color of the dots represents the mean position of the states away from the mirror plane, where red denotes the surface states and yellow represents the bulk states. By utilizing the mirror operator, we can evaluate the mirror Hall conductance using Eq. (8). In Fig. 4c, we illustrate the mirror Hall conductance as a function of the chemical potential for several slab thickness L_x . Notably, when chemical potential resides within the bulk band gap and crosses the gapless Dirac surface states, and the slab thickness is sufficient, the mirror Hall conductivity is quantized to be -1 . This result is consistent with the analysis presented above.

Another way to grow a thin film with mirror symmetry is to make use of twin boundaries in crystal^{70–72}. A twin plane is planar stacking faults in a fixed crystallographic direction (say, $[uvw]$) and usually has low formation energies. Structurally, it can be described as the reversal of atomic stacking sequence along the $[uvw]$ direction about the twin plane. We also use Bi₂Se₃ as an example to illustrate this approach. [001]-oriented slabs of the topological insulator Bi₂Se₃ do not possess mirror symmetry along the stacking direction. However, it is feasible to create a crystalline structure with mirror symmetry by incorporating a twin plane, as illustrated in Fig. 5a. The resulting mirror symmetry operator, denoted as \hat{M}_z , maps the crystal structure onto itself across the twin plane. Due to the imposed symmetry constraints (\hat{C}_{3z} , \hat{T} and \hat{M}_z), the hopping term between the nearest two layers across the mirror plane can only take the following form $\psi_{-1}^\dagger(r_{00}\sigma_0\tau_0 + r_{20}\sigma_0\tau_z + ir_{xz}\sigma_z\tau_x + ir_{y0}\sigma_0\tau_y)\psi_1 + \text{h.c.}$. Here, all the parameters involved are real. The band structure for this slab geometry is illustrated in Fig. 5b. The color of the dots represents the average position of the states away from the mirror plane. As indicated by the blue dots, the interface states are gapped out due to the presence of coupling, a consequence of the absence of surface states between two topologically nontrivial insulators. The gapless surface states appear only on the top and bottom exposed surfaces. We have

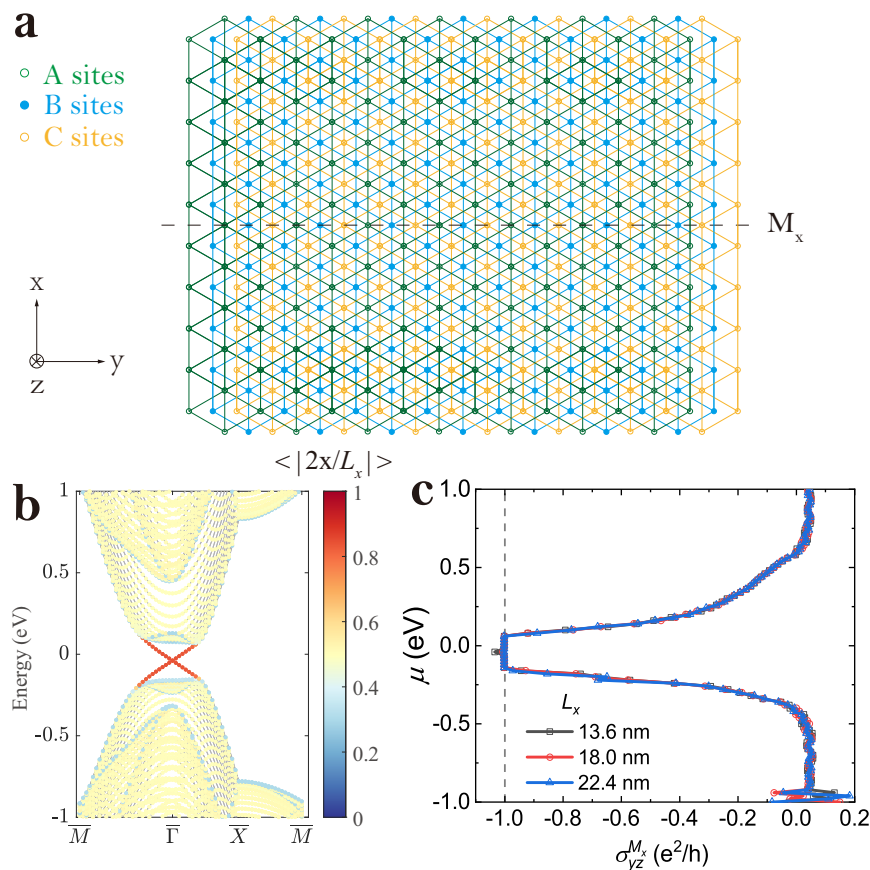


Fig. 4 | Results for Bi_2Se_3 in [100] direction. **a** The slab structure along the [100] direction of Bi_2Se_3 . The gray dashed line indicates the mirror plane M_x . **b** The band structure of the slab geometry along the high symmetry points of projected surface Brillouin zone: $\bar{M} \rightarrow \bar{\Gamma} \rightarrow \bar{X} \rightarrow \bar{M}$. The color of the dots represents the mean position of the states away from the mirror plane $\langle |2x/L_x| \rangle$, where the mirror plane is set at

$x=0$. Red dot denotes the surface states and yellow dot represents the bulk states, and the blue dot indicates the mirror surface states. **c** The mirror Hall conductivity $\sigma_{yz}^{M_x}$ as a function of the chemical potential μ for several slab thickness L_x . The accuracy of the Hall conductivity is controlled by the precision of the numerical integral, which can be improved by increasing the number of k-points over the Brillouin Zone.

also computed the mirror Hall conductivity for this structure. As depicted in Fig. 5c, the mirror Hall conductivity is quantized to -1 for various thicknesses L_z when chemical potential crosses the gapless Dirac surface states. As illustrated in Fig. 5d, we present the energy dispersion for the gapless Dirac band. A hexagonal warping term is permitted by the threefold rotation symmetry. Therefore, the energy dispersion exhibits a non-circular shape, resembling a snowflake pattern. In Fig. 5e, we plot the distribution of the mirror Berry curvature for four gapless bands, denoted as $\Omega_{M_z}(\mathbf{k}) = \sum_{\chi} \chi \Omega^{\chi}(\mathbf{k})$. Time-reversal symmetry relates the Berry curvature between the two mirror sectors, which can be expressed as $\hat{T} : \Omega^{\chi}(\mathbf{k}) \rightarrow -\Omega^{-\chi}(-\mathbf{k})$. As a consequence, we have $\Omega_{M_z}(\mathbf{k}) = \Omega_{M_z}(-\mathbf{k})$. This leads the mirror Berry curvature exhibiting six-fold symmetry under $\theta \rightarrow \theta + \pi/3$ due to \hat{C}_{3z} symmetry. However, the sum of the mirror Berry curvature for the four gapless Dirac bands over the first Brillouin zone (FBZ), which is the region enclosed by the gray dashed line, remains consistently quantized as -1 , in accordance with the aforementioned analysis. The mirror Hall conductivity plateau can be understood as follows: In parity invariant regime, when chemical potential μ intersects only the surface states, the line integrals of the Berry connection over the Fermi surface can be demonstrated as follows: $\oint_{\text{FS}} d\mathbf{k} \cdot \mathcal{A}_{\text{H}}^{\chi}(\mathbf{k}) = N\pi$ where N is an integer²⁶. Consequently, as μ varies across the surface states, the mirror Hall conductivity exhibits a plateau. The sample may also be made possibly by folding a TI thin film mechanically, which technique was extensively used in the field of 2D materials such as twisted graphene⁷³. Hence the slab with a twin plane is an ideal material candidate to realize the half-quantum mirror Hall effect.

Discussion

If the thickness of the TI film is reduced to that the wave functions of the top and bottom surface states have a spatial overlap, the surface states gap out, and induces a tiny gap E_g at the Γ point^{30,74}. A mirror Chern number can be well defined for the two gapped surface bands, $C_{\chi} = 0$ or χ . The nontrivial case has the mirror Hall conductivity $\sigma_{xy}^{M_z} = 2 \frac{e^2}{h}$, that is actually the quantum spin Hall effect. Even in this gapped case, if the chemical potential μ deviates from the energy gap E_g , it is found that the mirror Hall conductivity approaches to $\frac{e^2}{h}$ very quickly from 0 or $2 \frac{e^2}{h}$, which reflects the fact that the symmetry-breaking term near the mirror plane cooperates into the bands away from the low-energy dispersions of the surface states.

The topological robustness of the half-quantum mirror Hall effect in a mirror-symmetric topological insulator is safeguarded by time-reversal and mirror symmetries. The latter is a spatial symmetry and can be broken by surface roughness or the charge transfer from the substrate. Within the mirror operator's eigenbasis, symmetry-breaking manifests as an inter-sector coupling, characterized by the inter-mirror scattering length l_{M_z} that gauges the extent of symmetry disruption. As highlighted in the "transport signature" section, an increase in the inter-sector symmetry-breaking term causes a reduction in l_{M_z} and a corresponding invisibility of the observable transport phenomena associated with the half-quantum mirror Hall effect. Generally, when the symmetry is broken explicitly, the mirror Hall conductivity will deviate from the quantized value. As shown in Supplementary Note 4, we consider a

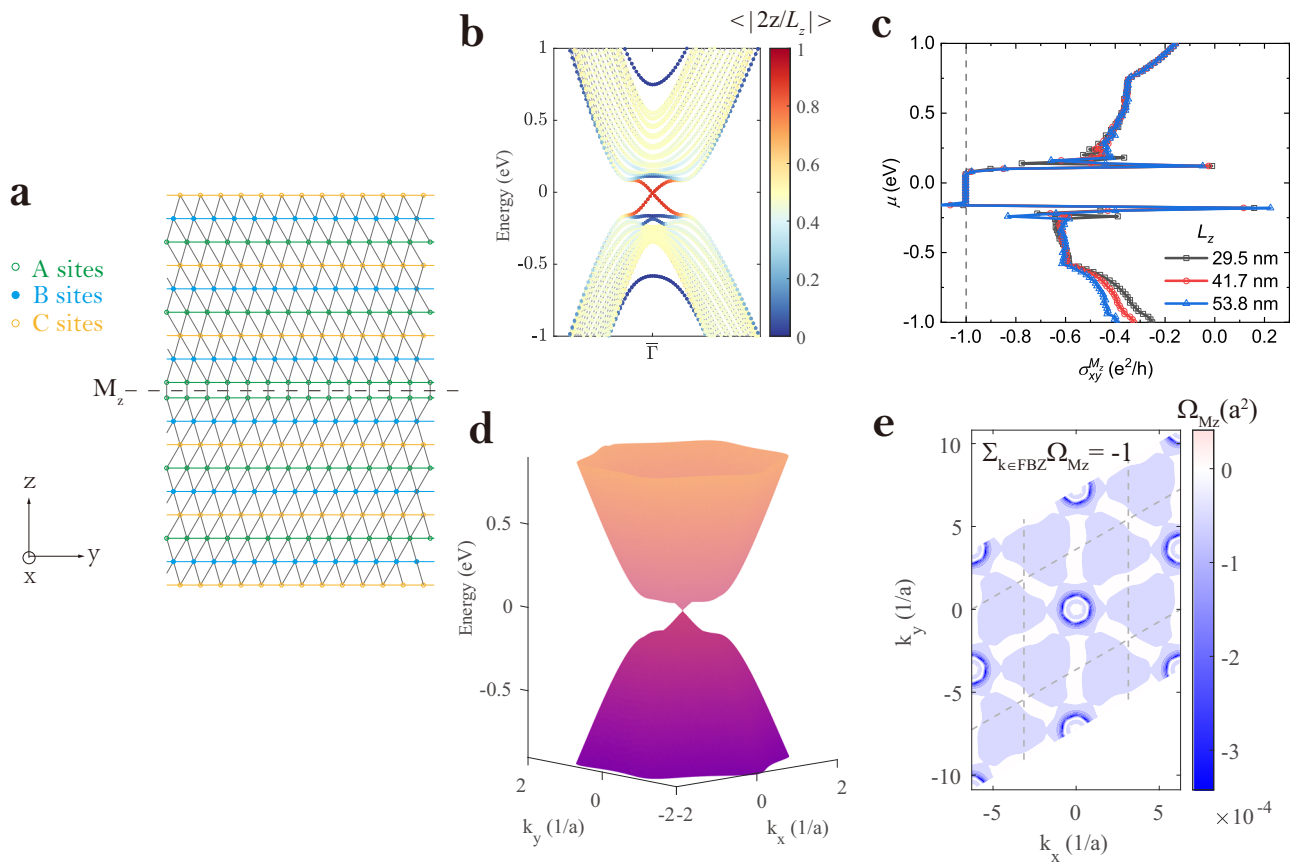


Fig. 5 | Results for Bi₂Se₃ in [001] direction with a twin boundary. **a** The twin boundary structure along the [001] direction of Bi₂Se₃. The gray dashed line indicates the mirror plane M_z for this twin boundary structure. **b** The band structure of the slab geometry around the Γ of projected surface Brillouin zone. The color of the dots represents the mean position of the states away from the mirror plane

$\langle |2z/L_z| \rangle$, where the mirror plane is set at $z=0$. **c** The mirror Hall conductivity σ_{xy}^M as a function of the chemical potential μ for several slab thickness L_z . **d** The dispersion of gapless Dirac bands. **e** The distribution of the mirror Berry curvature $\Omega_{M_z}(\mathbf{k}) = \sum_{\chi} \chi \Omega^{\chi}(\mathbf{k})$ for the four gapless Dirac bands. The region enclosed by the gray dashed line represents the first Brillouin zone.

special symmetry-breaking term that acts only on the bottom layer. It removes the degeneracy of the surface states on the top and bottom layer. However, as illustrated in Supplementary Fig. 3, we observe that mirror symmetry breaking on the surface layers has a minimal impact on the quantization of mirror Hall conductivity (approximated as $-e^2/h$) when the chemical potential intersects with the surface states. This is because the mirror Hall effect primarily originates from high-energy states located within the bulk of the material, and the surface potential does not significantly affect these states.

In summary, the half-quantum mirror Hall effect reveals a unique type of mirror-symmetry-induced quantum anomaly in a time-reversal invariant lattice TI film, giving rise to a topological metallic state of matter with time-reversal invariance.

Methods

Derivation of Gapless Dirac Cone Model with Parity Symmetry Breaking

We solve the Hamiltonian $\hat{H} = \hat{H}_{1d} + \hat{H}_{\parallel}$ by separating it into two parts: the parallel part is given by $\hat{H}_{\parallel} = \sum_{\mathbf{k}} \sum_z \hat{\psi}_{\mathbf{k},z}^{\dagger} \lambda_{\parallel} [\sin(k_x a) \sigma_x \tau_x + \sin(k_y b) \sigma_y \tau_x] \hat{\psi}_{\mathbf{k},z}$, and the one-dimensional (1-D) Hamiltonian part \hat{H}_{1d} , which is described by

$$\hat{H}_{1d} = \sum_{\mathbf{k}} \sum_z (\hat{\psi}_{\mathbf{k},z}^{\dagger} M_0(\mathbf{k}) \sigma_0 \tau_z \hat{\psi}_{\mathbf{k},z} + \hat{\psi}_{\mathbf{k},z}^{\dagger} T_{z,z+1} \hat{\psi}_{\mathbf{k},z+1} + \text{h.c.}). \quad (18)$$

The eigenvalue problem of the 1-D Hamiltonian with respect to boundary conditions is

$$\begin{cases} H_{1d}(\mathbf{k})|\Phi(\mathbf{k})\rangle = E(\mathbf{k})|\Phi(\mathbf{k})\rangle, \\ |\Phi(\mathbf{k}, \pm l/2)\rangle = 0, \end{cases} \quad (19)$$

where $l=L_z+1$ with L_z total sites number along z . $H_{1d}(\mathbf{k})$ takes the form of a block tridiagonal matrix in terms of the layer index with dimension as $4L_z \times 4L_z$, defined as $\hat{H}_{1d} = \sum_{\mathbf{k}} \hat{\Psi}_{\mathbf{k}}^{\dagger} H_{1d}(\mathbf{k}) \hat{\Psi}_{\mathbf{k}}$, where $\hat{\Psi}_{\mathbf{k}}$ represents the collective spinor encompassing all the layer components. Solving the set of equations above gives eigenstates read

$$\begin{aligned} \Phi_1(l_z) &= \begin{pmatrix} \varphi(+, l_z) \\ 0 \end{pmatrix}, \Phi_2(l_z) = \begin{pmatrix} 0 \\ \chi(-, l_z) \end{pmatrix}, \\ \Phi_3(l_z) &= \begin{pmatrix} \chi(+, l_z) \\ 0 \end{pmatrix}, \Phi_4(l_z) = \begin{pmatrix} 0 \\ \varphi(-, l_z) \end{pmatrix}, \end{aligned} \quad (20)$$

where

$$\begin{cases} \varphi(s, l_z) = C \begin{pmatrix} -is\lambda_{\perp} f_{+}(l_z) \\ t_{\perp} \eta f_{-}(l_z) \end{pmatrix}, E \\ \chi(s, l_z) = C \begin{pmatrix} t_{\perp} \eta f_{-}(l_z) \\ is\lambda_{\perp} f_{+}(l_z) \end{pmatrix}, -E \end{cases}, \quad (21)$$

with C the norm, and $\pm E$ refer to corresponding eigenvalue which could be solved consistently in a closed manner with equations

$$\begin{cases} E = M + 2t_{\perp} \frac{\cos \xi_1 g(\xi_1) - \cos \xi_2 g(\xi_2)}{g(\xi_1) - g(\xi_2)}, \\ \cos \xi_{\alpha} = \frac{-Mt_{\perp} + (-1)^{\alpha-1} \sqrt{M^2 t_{\perp}^2 - (t_{\perp}^2 - \lambda_{\perp}^2/4)(M^2 + \lambda_{\perp}^2 - E^2)}}{2(t_{\perp}^2 - \lambda_{\perp}^2/4)}, \end{cases} \quad (22)$$

where $\alpha = 1, 2$ and M is referred to $M_0(\mathbf{k})$. For definitions of f_{\pm} and η , please refer to the Supplementary Information.

Our solution is exact with \mathbf{k} -dependence and includes all solutions $E_n(\mathbf{k})$, $n = 1, \dots, L_z$, with $n = 1$ denoting possible non-trivial zero-mode state. Then by projecting the original Hamiltonian onto the obtained $4L_z$ eigenstates, we get the effective Hamiltonian

$$H_{\text{EFF}}(\mathbf{k}) = \bigoplus_{n=1}^{L_z} \left[\lambda_{\parallel} (\sin(k_x a) \tilde{\sigma}_x + \sin(k_y b) \tilde{\sigma}_y) \tilde{\tau}_0 + E_n \tilde{\sigma}_z \tilde{\tau}_z \right] = \bigoplus_{n,\chi} h_{n,\chi}(\mathbf{k}), \quad (23)$$

where $\chi = \pm$ is the mirror label, and due to the explicit direct sum form, we separate $n = 1$ block and make equivalence with

$$H_{\text{surf},\chi} = h_{1,\chi} = \lambda_{\parallel} (\sin(k_x a) \tilde{\sigma}_x + \sin(k_y b) \tilde{\sigma}_y) + \chi \Delta(\mathbf{k}) \tilde{\sigma}_z, \quad \Delta(\mathbf{k}) \equiv E_1(\mathbf{k}), \quad (24)$$

which is Eq. (2) in the main text. Meanwhile, it could be proved (please refer to the Supplementary Information) that in the thick limit,

$$\Delta(\mathbf{k}) \simeq \Theta(-m_0(\mathbf{k})) m_0(\mathbf{k}). \quad (25)$$

Charge transport associated with the half-quantum mirror Hall effect

In this section, we present the macroscopic theory for the transport properties associated with the half-quantum mirror Hall effect. The generalized Ohm's law for currents from two Mirror eigenstates:

$$J_{\chi,i}(\mathbf{r}) = -\sigma_{ij}^{\chi} \partial_j \phi(\mathbf{r}) + e D_{ij}^{\chi} \partial_j \delta n_{\chi}(\mathbf{r})$$

where $\phi(\mathbf{r})$ is the electric potential, $i, j = x, y$ are spatial coordinates, $\delta n_{\chi}(\mathbf{r})$ is the variation of the charge density in mirror sector χ due to the transport, σ_{ij}^{χ} is the homogeneous conductivity tensor, and D_{ij}^{χ} is the corresponding diffusion coefficient tensor. A repeated spatial index obeys Einstein's summation convention. The first and second terms on the right-hand side are the drift current due to the electric field and the diffusion current due to the inhomogeneity of the electron density. The diffusion constant D_{ij}^{χ} is given by the Einstein relation $e^2 D_{ij}^{\chi} = \sigma_{ij}^{\chi} S^X$ where $S^X = \partial \mu_{\chi} / \partial n_{\chi} = \nu_{\chi}^{-1}$ is the static stiffness and ν_{χ} is the thermodynamics density of state or the compressibility. We have neglected the inter-mirror interaction such that the inter-mirror elements of the conductivity and stiffness matrices vanish. We can define the total charge density (c) $\delta n_c(\mathbf{r}) = \sum_{\chi} \delta n_{\chi}(\mathbf{r})$ and the mirror polarization density (M_z) $\delta n_{M_z}(\mathbf{r}) = \sum_{\chi} \chi \delta n_{\chi}(\mathbf{r})$. Similarly, the total charge current density is determined by $J_{c,i} = \sum_{\chi} J_{\chi,i}$ and the total mirror current density is $J_{M_z,i} = \sum_{\chi} \chi J_{\chi,i}$ which can be obtained as

$$\begin{aligned} J_{c,i} &= \delta_{ij} \left(-\sigma_c \partial_j \phi + e D_c \partial_j \delta n_c \right) + e D_H^{M_z} \epsilon_{ij} \partial_j \delta n_{M_z}, \\ J_{M_z,i} &= \delta_{ij} D_c \partial_j \delta n_{M_z} + \epsilon_{ij} \left(-\sigma_H^{M_z} \partial_j \phi + e D_H^{M_z} \partial_j \delta n_c \right), \end{aligned} \quad (26)$$

where we have introduced the longitudinal charge conductivity $\sum_{\chi} \sigma_{ij}^{\chi} = \delta_{ij} \sigma_c$, the mirror Hall conductivity $\sum_{\chi} \chi \sigma_{ij}^{\chi} = \epsilon_{ij} \sigma_H^{M_z}$, the longitudinal charge diffusion constant $\frac{1}{2} \sum_{\chi} D_{ij}^{\chi} = \delta_{ij} D_c$, and the mirror Hall

diffusion constant $\frac{1}{2} \sum_{\chi} \chi D_{ij}^{\chi} = \epsilon_{ij} D_H^{M_z}$ with δ_{ij} and ϵ_{ij} as the Kronecker delta and Levi-Civita symbols. Equation (26) establish a linear relationship between the densities and currents in the presence of the electric potential. To solve these equations, we also require the two continuity equations:

$$\begin{aligned} \partial_j J_{c,i} &= 0, \\ \partial_j J_{M_z,i} &= e \delta n_{M_z} / \tau_{M_z} \end{aligned}$$

where τ_{M_z} is a phenomenological relaxation time due to the inter-mirror scattering which equilibrates the two mirror sectors relaxing the system to a steady state. By combining the continuity equation with Eq. (26), we can obtain the electric field inside the system obeys the Laplace equation $\nabla^2 \phi = 0$ and a diffusion equation for the mirror polarization density

$$D_c \nabla^2 \delta n_{M_z} = \frac{\delta n_{M_z}}{\tau_{M_z}} - \nabla \times \left(-\frac{\sigma_H^{M_z}}{e} \nabla \phi + D_H^{M_z} \nabla \delta n_c \right) \cdot \hat{z}. \quad (27)$$

We use the local charge neutrality constraint $\delta n_c \approx 0$ and $\nabla \times (\sigma_H^{M_z} \nabla \phi) = \sigma_H^{M_z} E_y [\delta(x - W/2) - \delta(x + W/2)]$ takes a delta-function value at the boundary between topologically non-trivial and trivial (vacuum) regions where $E_i = -\partial_i \phi$ is the electric field. The general solution for the diffusion equation is

$$\delta n_{M_z}(\mathbf{r}) = A e^{-x/l_{M_z}} + B e^{x/l_{M_z}}$$

with $l_{M_z} = \sqrt{D_c \tau_{M_z}}$ the mirror diffusion length. This equation needs to be supplemented by suitable boundary conditions. Here, we consider a two-terminal transport measurement and a charge current is driven between injector and collector electrodes by the electric field. In this situation, the boundary condition is on the mirror current density $J_{M_z,x}(x = \pm W/2, y) = 0$ which implies that no mirror current can flow outside the sample. By combining with Eq. (26), we can obtain the boundary constraint on the mirror polarization density

$$\left(\partial_x \delta n_{M_z} - \frac{\tan \theta_{M_z}}{1 + \tan^2 \theta_{M_z}} \frac{J_{c,y}}{D_c} \right) \Big|_{x = \pm W/2} = 0$$

where $\theta_{M_z} = \tan^{-1}(\sigma_H^{M_z} / \sigma_c)$ is the mirror Hall angle. By solving the differential equations with the boundary conditions, we arrive the polarization density in Eq. (10) and the charge current density in Eq. (11) For a multi-terminal measurement illustrated in the lower panel of Fig. 3b, the current I is applied along the y -direction, flowing from terminal 8 to terminal 2. We impose periodic boundary conditions in the x -direction. Then the problem can be solved by Fourier transforming all the physical quantities in the x -direction $\tilde{f}(k, y) = \int_{-\infty}^{\infty} dx e^{-ikx} f(x, y)$. Within a conductor at electrostatic equilibrium, the electric potential ϕ satisfies the Laplace equation $\nabla^2 \phi = 0$. Furthermore, in accordance with the diffusion equation [Eq. (27)], we can assume the solutions of the form $\tilde{\phi}(k, y) = a \cosh(ky) + b \sinh(ky)$ for the potential, and $\delta \tilde{n}_{M_z}(k, y) = c \cosh(\omega(k)y) + d \sinh(\omega(k)y)$ for the mirror polarization density where $\omega(k) = \sqrt{k^2 + l_{M_z}^{-2}}$. By using the boundary conditions for the charge current density $J_{c,y}(x, y = \pm \frac{L}{2}) = \frac{I}{W} \Theta(\frac{W}{2} - |x|)$ and mirror current density $J_{M_z,y}(x, y = \pm \frac{L}{2}) = 0$, we can obtain the resistance as a function of the probe position x according to the fundamental definition $R(x) = [\phi(x, \frac{L}{2}) - \phi(x, -\frac{L}{2})] / I$

$$R(x) = \frac{2}{\sigma_c} \int \frac{dk}{2\pi} \frac{e^{ikx} \sin(\frac{kW}{2}) / (kW/2) \omega(k)}{\omega(k) k \coth(\frac{kL}{2}) + k^2 \tan^2(\theta_{M_z}) \coth(\frac{\omega(k)L}{2})}. \quad (28)$$

In two limiting regimes, we derive the analytical expressions for non-local resistivity in Eq. (13) and for the resistivity as given in Eq. (14) when current injection and voltage measurement are conducted on the same terminals.

Tight-binding model for Bi₂Se₃ and Bi₂Te₃

The tight-binding models for Bi₂Se₃ and Bi₂Te₃ are constructed using Wannier functions of the conduction and valence bands, primarily described by a set of few effective states $|\Lambda^{\tau} j_z\rangle$. Here, τ is the state parity, j_z is the z -axis projection of the total angular momentum, and Λ labels the orbital contributions from Bi and Se(Te) atoms. Based on first principle studies, the states around the Fermi surface are $|P1^{\pm}, \pm\frac{1}{2}\rangle$, $|P2^{\pm}, \pm\frac{1}{2}\rangle$, $|P2^{\pm}, \tilde{\Gamma}_4\rangle$, $|P2^{\pm}, \tilde{\Gamma}_5\rangle$, and $|P2^{\pm}, \pm\frac{1}{2}\rangle$. Among these states, $|P1^{\pm}, \pm\frac{1}{2}\rangle$, $|P2^{\pm}, \pm\frac{1}{2}\rangle$ are responsible for the band inversion^{40,69}. Therefore, in our calculations, we only focus on these four bases, as the bulk and surface bands are already capable of accurately reproducing the essential features predicted by first-principles studies⁶⁹. Additional bases such as $|P2^{\pm}, \tilde{\Gamma}_4\rangle$, $|P2^{\pm}, \tilde{\Gamma}_5\rangle$, $|P2^{\pm}, \pm\frac{1}{2}\rangle$ can be included to improve the fit. The form of the Hamiltonian is highly constrained by crystal symmetries, including threefold rotation symmetry \hat{C}_{3z} along the z axis, twofold rotation symmetry \hat{C}_{2x} along the x -axis, inversion symmetry \hat{P} , and time-reversal symmetry \hat{T} . Symmetry considerations allow us to reduce the number of the model parameters to 10 independent ones. These parameters can be determined by least-square fitting the bulk band structure obtained from the DFT calculations. The Hamiltonian H_{tb} consists of an interlayer and intralayer part: $H_{\text{tb}} = H_{\text{intra}} + H_{\text{inter}}$ ⁶⁹, where

$$H_{\text{intra}} = \sum_{\mathbf{r}} \left\{ \psi_{\mathbf{r}}^{\dagger} \left(\frac{\epsilon_1 + \epsilon_3}{2} \sigma_0 \tau_0 + \frac{\epsilon_1 - \epsilon_3}{2} \sigma_0 \tau_z \right) \psi_{\mathbf{r}} + \sum_{\nu=1,2,3} \left[\psi_{\mathbf{r}+\mathbf{a}_{\nu}}^{\dagger} \left(\frac{t_a^{11} + t_a^{33}}{2} \sigma_0 \tau_0 + \frac{t_a^{11} - t_a^{33}}{2} \sigma_0 \tau_z - it_a^{13} \sigma_z \tau_x + \frac{i}{a} t_a^{14} \epsilon_{ijk} \mathbf{a}_{\nu,i} \sigma_j^{\dagger} \tau_x \right) \psi_{\mathbf{r}} + h.c. \right] \right\}$$

$$H_{\text{inter}} = \sum_{\mathbf{r}} \sum_{\nu=1,2,3} \left[\psi_{\mathbf{r}+\mathbf{b}_{\nu}}^{\dagger} \left(\frac{t_b^{11} + t_b^{33}}{2} \sigma_0 \tau_0 + \frac{t_b^{11} - t_b^{33}}{2} \sigma_0 \tau_z + it_b^{13} \sigma_0 \tau_y + i \frac{\sqrt{3}}{a} t_b^{14} \epsilon_{ijk} \mathbf{b}_{\nu,i} \sigma_j^{\dagger} \tau_x \right) \psi_{\mathbf{r}} + h.c. \right]$$

Here \mathbf{r} labels the site. The vectors $\psi_{\mathbf{r}} = (|P1^{\pm}, +\frac{1}{2}\rangle, |P2^{\pm}, +\frac{1}{2}\rangle, |P1^{\pm}, -\frac{1}{2}\rangle, |P2^{\pm}, -\frac{1}{2}\rangle)^T$ correspond to the two spins and two orbits. The notation $\pm \mathbf{a}_{\nu}$ represents the 6 intralayer nearest neighbor vectors of each triangular lattice, namely, $\mathbf{a}_1 = (a, 0, 0)$, $\mathbf{a}_2 = (-a/2, \sqrt{3}a/2, 0)$, $\mathbf{a}_3 = (-a/2, -\sqrt{3}a/2, 0)$. Similarly, $\pm \mathbf{b}_{\nu}$ denotes the 6 interlayer nearest neighbors vectors, $\mathbf{b}_1 = (0, \sqrt{3}a/3, c/3)$, $\mathbf{b}_2 = (-a/2, -\sqrt{3}a/6, c/3)$, $\mathbf{b}_3 = (a/2, -\sqrt{3}a/6, c/3)$ with $a = 4.14 \text{ \AA}$ and $c = 28.70 \text{ \AA}$ for Bi₂Se₃. In the Hamiltonian, ϵ_1 and ϵ_3 represent the on-site potentials for two orbits; t_a^{11} and t_a^{33} are the spin-independent intraorbit and intralayer hopping terms. t_b^{11} (t_b^{33}) and t_b^{13} are the spin-independent intraorbit and inter orbit interlayer hopping terms, respectively. t_a^{14} and t_b^{14} are spin-dependent intra- and interlayer hopping respectively. t_a^{13} is responsible for the hexagonal warping effects of Dirac surface states. For Bi₂Se₃, the obtained parameters are $\epsilon_1 = 1.602$, $\epsilon_3 = -1.374$, $t_a^{11} = -0.240$, $t_a^{33} = 0.211$, $t_b^{11} = -0.067$, $t_b^{33} = 0.04$, $t_b^{13} = 0.210$, $t_a^{14} = -0.17$, $t_b^{14} = 0.045$, and $t_b^{13} = -0.19$, all given in the units of eV, adopted from ref. 69.

Data availability

All data generated or analyzed during this study are included in this published article (and its Supplementary Information files).

References

- Niemi, A. J. & Semenoff, G. W. Axial-anomaly-induced fermion fractionalization and effective gauge-theory actions in odd-dimensional space-times. *Phys. Rev. Lett.* **51**, 2077 (1983).
- Redlich, A. N. Gauge noninvariance and parity nonconservation of three-dimensional Fermions. *Phys. Rev. Lett.* **52**, 18 (1984).
- Neto, A. C., Guinea, F., Peres, N. M., Novoselov, K. S. & Geim, A. K. The electronic properties of graphene. *Rev. Mod. Phys.* **81**, 109 (2009).
- Hasan, M. Z. & Kane, C. L. Colloquium: topological insulators. *Rev. Mod. Phys.* **82**, 3045 (2010).
- Qi, X.-L. & Zhang, S.-C. Topological insulators and superconductors. *Rev. Mod. Phys.* **83**, 1057 (2011).
- Shen, S.-Q. *Topological Insulators*, 2nd ed., Vol. 187 (Springer, Singapore, 2017).
- Fradkin, E., Dagotto, E. & Boyanovsky, D. Physical realization of the parity anomaly in condensed matter physics. *Phys. Rev. Lett.* **57**, 2967 (1986).
- Haldane, F. D. M. Model for a Quantum Hall Effect without Landau Levels. *Phys. Rev. Lett.* **61**, 2015 (1988).
- Qi, X.-L., Hughes, T. L. & Zhang, S.-C. Topological field theory of time-reversal invariant insulators. *Phys. Rev. B* **78**, 195424 (2008).
- Yu, R. et al. Quantized anomalous Hall effect in magnetic topological insulators. *Science* **329**, 61 (2010).
- Qiao, Z. et al. Quantum anomalous Hall effect in graphene from Rashba and exchange effects. *Phys. Rev. B* **82**, 161414 (2010).
- Chu, R.-L., Shi, J. & Shen, S.-Q. Surface edge state and half-quantized Hall conductance in topological insulators. *Phys. Rev. B* **84**, 085312 (2011).
- Li, J. et al. Intrinsic magnetic topological insulators in van der Waals layered MnBi₂Te₄-family materials. *Sci. Adv.* **5**, eaaw5685 (2019).
- Chang, C.-Z. et al. Experimental observation of the quantum anomalous Hall effect in a magnetic topological insulator. *Science* **340**, 167 (2013).
- Checkelsky, J. et al. Trajectory of the anomalous Hall effect towards the quantized state in a ferromagnetic topological insulator. *Nat. Phys.* **10**, 731 (2014).
- Kou, X. et al. Scale-invariant quantum anomalous Hall effect in magnetic topological insulators beyond the two-dimensional limit. *Phys. Rev. Lett.* **113**, 137201 (2014).
- Deng, Y. et al. Quantum anomalous Hall effect in intrinsic magnetic topological insulator MnBi₂Te₄. *Science* **367**, 895 (2020).
- Liu, C. et al. Robust axion insulator and Chern insulator phases in a two-dimensional antiferromagnetic topological insulator. *Nat. Mater.* **19**, 522 (2020).
- Zhang, S. et al. Anomalous quantization trajectory and parity anomaly in Co cluster decorated BiSbTeSe₂ nanodevices. *Nat. Commun.* **8**, 977 (2017).
- Böttcher, J., Tutschku, C., Molenkamp, L. W. & Hankiewicz, E. Survival of the quantum anomalous Hall effect in orbital magnetic fields as a consequence of the parity anomaly. *Phys. Rev. Lett.* **123**, 226602 (2019).
- Fang, C. & Fu, L. New classes of topological crystalline insulators having surface rotation anomaly. *Sci. Adv.* **5**, eaat2374 (2019).
- Mogi, M. et al. Experimental signature of the parity anomaly in a semi-magnetic topological insulator. *Nat. Phys.* **18**, 390 (2022).
- Wang, H.-W., Fu, B. & Shen, S.-Q. Helical symmetry breaking and quantum anomaly in massive Dirac fermions. *Phys. Rev. B* **104**, L241111 (2021).
- Fu, B., Zou, J.-Y., Hu, Z.-A., Wang, H.-W. & Shen, S.-Q. Quantum anomalous semimetals. *npj Quantum Mater.* **7**, 94 (2022).
- Zou, J.-Y., Fu, B., Wang, H.-W., Hu, Z.-A. & Shen, S.-Q. Half-quantized Hall effect and power law decay of edge-current distribution. *Phys. Rev. B* **105**, L201106 (2022).
- Zou, J.-Y. et al. Half-quantized Hall effect at the parity-invariant Fermi surface. *Phys. Rev. B* **107**, 125153 (2023).
- Zhou, H. et al. Transport theory of half-quantized Hall conductance in a semimagnetic topological insulator. *Phys. Rev. Lett.* **129**, 096601 (2022).
- Yang, H., Song, L., Cao, Y. & Yan, P. Realization of Wilson fermions in topolectrical circuits. *Commun. Phys.* **6**, 211 (2023).

29. Fu, L., Kane, C. L. & Mele, E. J. Topological insulators in three dimensions. *Phys. Rev. Lett.* **98**, 106803 (2007).
30. Lu, H.-Z., Shan, W.-Y., Yao, W., Niu, Q. & Shen, S.-Q. Massive Dirac fermions and spin physics in an ultrathin film of topological insulator. *Phys. Rev. B* **81**, 115407 (2010).
31. Hori, K. *Mirror symmetry*, Vol. **1** (American Mathematical Soc., 2003).
32. Teo, J. C., Fu, L. & Kane, C. Surface states and topological invariants in three-dimensional topological insulators: Application to $\text{Bi}_{1-x}\text{Sb}_x$. *Physical Review B* **78**, 045426 (2008).
33. Fu, L. Topological crystalline insulators. *Phys. Rev. Lett.* **106**, 106802 (2011).
34. Hsieh, T. H. et al. Topological crystalline insulators in the SnTe material class. *Nat. Commun.* **3**, 982 (2012).
35. Chiu, C.-K. & Schnyder, A. P. Classification of reflection-symmetry-protected topological semimetals and nodal superconductors. *Phys. Rev. B* **90**, 205136 (2014).
36. Ando, Y. & Fu, L. Topological crystalline insulators and topological superconductors: from concepts to materials. *Annu. Rev. Condens. Matter Phys.* **6**, 361 (2015).
37. Kane, C. L. & Mele, E. J. Quantum spin Hall effect in graphene. *Phys. Rev. Lett.* **95**, 226801 (2005).
38. Bernevig, B. A., Hughes, T. L. & Zhang, S.-C. Quantum spin Hall effect and topological phase transition in HgTe quantum wells. *Science* **314**, 1757 (2006).
39. Zhang, H. et al. Topological insulators in Bi_2Se_3 , Bi_2Te_3 and Sb_2Te_3 with a single Dirac cone on the surface. *Nat. Phys.* **5**, 438 (2009).
40. Liu, C.-X. et al. Model Hamiltonian for topological insulators. *Phys. Rev. B* **82**, 045122 (2010).
41. Li, R., Wang, J., Qi, X.-L. & Zhang, S.-C. Dynamical axion field in topological magnetic insulators. *Nat. Phys.* **6**, 284 (2010).
42. Sekine, A. & Nomura, K. Axionic antiferromagnetic insulator phase in a correlated and spin-orbit coupled system. *J. Phys. Soc. Jpn.* **83**, 104709 (2014).
43. König, M. et al. The quantum spin Hall effect: Theory and experiment. *J. Phys. Soc. Jpn.* **77**, 031007 (2008).
44. Nielsen, H. B. & Ninomiya, M. A no-go theorem for regularizing chiral fermions. *Phys. Lett. B* **105**, 219 (1981).
45. Creutz, M. & Horváth, I. Surface states and chiral symmetry on the lattice. *Phys. Rev. D* **50**, 2297 (1994).
46. Mahan, G. *Many-particle physics* (Plenum Press, New York, NY, 1981).
47. Murakami, S. Quantum spin Hall effect and enhanced magnetic response by spin-orbit coupling. *Phys. Rev. Lett.* **97**, 236805 (2006).
48. Yang, M.-F. & Chang, M.-C. Středa-like formula in the spin Hall effect. *Phys. Rev. B* **73**, 073304 (2006).
49. Haldane, F. D. M. Berry Curvature on the Fermi Surface: Anomalous Hall Effect as a Topological Fermi-Liquid Property. *Phys. Rev. Lett.* **93**, 206602 (2004).
50. Hirsch, J. Spin Hall Effect. *Phys. Rev. Lett.* **83**, 1834 (1999).
51. Brüne, C. et al. Evidence for the ballistic intrinsic spin Hall effect in HgTe nanostructures. *Nat. Phys.* **6**, 448 (2010).
52. Balakrishnan, J., Kok Wai Koon, G., Jaiswal, M., Castro Neto, A. & Özyilmaz, B. Colossal enhancement of spin-orbit coupling in weakly hydrogenated graphene. *Nat. Phys.* **9**, 284 (2013).
53. Sinova, J., Valenzuela, S. O., Wunderlich, J., Back, C. & Jungwirth, T. Spin Hall effects. *Rev. Mod. Phys.* **87**, 1213 (2015).
54. Kondou, K. et al. Fermi-level-dependent charge-to-spin current conversion by Dirac surface states of topological insulators. *Nat. Phys.* **12**, 1027 (2016).
55. Abanin, D. et al. Giant nonlocality near the Dirac point in graphene. *Science* **332**, 328 (2011).
56. Shimazaki, Y. et al. Generation and detection of pure valley current by electrically induced Berry curvature in bilayer graphene. *Nat. Phys.* **11**, 1032 (2015).
57. Yamamoto, M., Shimazaki, Y., Borzenets, I. V. & Tarucha, S. Valley Hall effect in two-dimensional hexagonal lattices. *J. Phys. Soc. Jpn.* **84**, 121006 (2015).
58. Abanin, D., Shytov, A., Levitov, L. & Halperin, B. Nonlocal charge transport mediated by spin diffusion in the spin Hall effect regime. *Phys. Rev. B* **79**, 035304 (2009).
59. Beconcini, M., Taddei, F. & Polini, M. Nonlocal topological valley transport at large valley Hall angles. *Phys. Rev. B* **94**, 121408 (2016).
60. Song, J. C. & Vignale, G. Low-dissipation edge currents without edge states. *Phys. Rev. B* **99**, 235405 (2019).
61. Sekine, A. & MacDonald, A. H. Valley pumping via edge states and the nonlocal valley Hall effect in two-dimensional semiconductors. *Phys. Rev. B* **102**, 155205 (2020).
62. Ziegler, K. Robust transport properties in graphene. *Phys. Rev. Lett.* **97**, 266802 (2006).
63. Ostrovsky, P., Gornyi, I. & Mirlin, A. Electron transport in disordered graphene. *Phys. Rev. B* **74**, 235443 (2006).
64. Bolotin, K. I., Sikes, K. J., Hone, J., Stormer, H. L. & Kim, P. Temperature-dependent transport in suspended graphene. *Phys. Rev. Lett.* **101**, 096802 (2008).
65. Du, X., Skachko, I., Barker, A. & Andrei, E. Y. Approaching ballistic transport in suspended graphene. *Nat. Nanotechnol.* **3**, 491 (2008).
66. Assaf, B. A. et al. Quantum coherent transport in SnTe topological crystalline insulator thin films. *Appl. Phys. Lett.* **105**, 102108 (2014).
67. Hossain, M. et al. Zahid Transport response of topological hinge modes in $\alpha - \text{Bi}_4\text{Br}_4$, *Nat. Phys.*, in press (2023).
68. Nakajima, S. The crystal structure of $\text{Bi}_2\text{Te}_{3-x}\text{Se}_x$. *J. Phys. Chem. Solids* **24**, 479 (1963).
69. Acosta, C. M. et al. Tight-binding model for the band dispersion in rhombohedral topological insulators over the whole Brillouin zone. *Phys. Rev. B* **98**, 035106 (2018).
70. Authier, A. *International tables for crystallography: Volume D: Physical properties of crystals* (Wiley Online Library, 2003).
71. Medlin, D., Ramasse, Q., Spataru, C. & Yang, N. Structure of the (0001) basal twin boundary in Bi_2Te_3 . *J. Appl. Phys.* **108**, 043517 (2010).
72. Lu, K. Stabilizing nanostructures in metals using grain and twin boundary architectures. *Nat. Rev. Mater.* **1**, 16019 (2016).
73. Cao, Y. et al. Unconventional superconductivity in magic-angle graphene superlattices. *Nature* **556**, 43 (2018).
74. Linder, J., Yokoyama, T. & Sudbø, A. Anomalous finite size effects on surface states in the topological insulator Bi_2Se_3 . *Phys. Rev. B* **80**, 205401 (2009).

Acknowledgements

This work was supported by the National Key R&D Program of China under Grant No. 2019YFA0308603, the Research Grants Council, University Grants Committee, Hong Kong under Grant Nos. C7012-21G and 17301823, and Guangdong Basic and Applied Basic Research Foundation No. 2024A1515010430 and 2023A1515140008.

Author contributions

S.Q.S. conceived the project. B.F. and K.Z.B. performed the theoretical analysis and simulation. B.F. and S.Q.S. wrote the manuscript with inputs from all authors. All authors contributed to the discussion of the results.

Competing interests

The authors declare no competing interests.

Additional information

Supplementary information The online version contains supplementary material available at <https://doi.org/10.1038/s41467-024-51215-x>.

Correspondence and requests for materials should be addressed to Shun-Qing Shen.

Peer review information *Nature Communications* thanks Su-Yang Xu, and the other, anonymous, reviewer(s) for their contribution to the peer review of this work. A peer review file is available.

Reprints and permissions information is available at <http://www.nature.com/reprints>

Publisher's note Springer Nature remains neutral with regard to jurisdictional claims in published maps and institutional affiliations.

Open Access This article is licensed under a Creative Commons Attribution-NonCommercial-NoDerivatives 4.0 International License, which permits any non-commercial use, sharing, distribution and reproduction in any medium or format, as long as you give appropriate credit to the original author(s) and the source, provide a link to the Creative Commons licence, and indicate if you modified the licensed material. You do not have permission under this licence to share adapted material derived from this article or parts of it. The images or other third party material in this article are included in the article's Creative Commons licence, unless indicated otherwise in a credit line to the material. If material is not included in the article's Creative Commons licence and your intended use is not permitted by statutory regulation or exceeds the permitted use, you will need to obtain permission directly from the copyright holder. To view a copy of this licence, visit <http://creativecommons.org/licenses/by-nc-nd/4.0/>.

© The Author(s) 2024